



## Article

# Experiences from Large-Scale Forest Mapping of Sweden Using TanDEM-X Data

Henrik J. Persson <sup>1,\*</sup> , Håkan Olsson <sup>1</sup>, Maciej J. Soja <sup>2,3</sup> , Lars M.H. Ulander <sup>4</sup> and Johan E.S. Fransson <sup>1</sup>

<sup>1</sup> Swedish University of Agricultural Sciences (SLU), Department of Forest Resource Management, Umeå 901 83, Sweden; hakan.olsson@slu.se (H.O.); johan.fransson@slu.se (J.E.S.F.)

<sup>2</sup> Horizon Geoscience Consulting, Belrose, NSW 2085, Australia; maciej.soja@utas.edu.au

<sup>3</sup> School of Land and Food, University of Tasmania, Hobart, TAS 7001, Australia

<sup>4</sup> Chalmers University of Technology, Department of Space, Earth and Environment, Microwave and Optical Remote Sensing, Gothenburg 412 96, Sweden; lars.ulander@chalmers.se

\* Correspondence: henrik.persson@slu.se; Tel.: +46-90-786-8105

Received: 12 October 2017; Accepted: 28 November 2017; Published: 2 December 2017

**Abstract:** This paper report experiences from the processing and mosaicking of 518 TanDEM-X image pairs covering the entirety of Sweden, with two single map products of above-ground biomass (AGB) and forest stem volume (VOL), both with 10 m resolution. The main objective was to explore the possibilities and overcome the challenges related to forest mapping extending a large number of adjacent satellite scenes. Hence, numerous examples are presented to illustrate challenges and possible solutions. To derive the forest maps, the observables backscatter, interferometric phase height and interferometric coherence, obtained from TanDEM-X, were evaluated using empirical robust linear regression models with reference data extracted from 2288 national forest inventory plots with a 10 m radius. The interferometric phase height was the single most important observable, to predict AGB and VOL. The mosaics were evaluated on different datasets with field-inventoried stands across Sweden. The root mean square error (RMSE) was about 21%–25% (27–30 tons/ha and 52–65 m<sup>3</sup>/ha) at the stand level. It was noted that the most influencing factors on the observables in this study were local temperature and geolocation errors that were challenging to robustly compensate against. Because of this variability at the scene-level, determinations of AGB and VOL for single stands are recommended to be used with care, as an equivalent accuracy is difficult to achieve for all different scenes, with varying acquisition conditions. Still, for the evaluated stands, the mosaics were of sufficient accuracy to be used for forest management at the stand level.

**Keywords:** TanDEM-X; forest; mosaic; synthetic aperture radar; volume; biomass; modelling

## 1. Introduction

The amount of remote sensing data of the Earth is increasing, and moreover, the quality of the collected data increases. For forest-related purposes, field inventories paired with airborne laser scanning (ALS) data have made forest maps of several vital variables, e.g., tree height, basal area, above-ground biomass (AGB) and stem volume (VOL), of yet unprecedented accuracy available [1–3]. AGB and VOL are strongly correlated, although AGB also includes the branches and is more commonly used in climate modelling, while the industry and forest owners tend to use VOL, as this is a metric of the merchantable forest products [4]. Airborne techniques (including photogrammetry) are both highly accurate, but also expensive for frequent usage, especially at larger scales. Satellite-based techniques have the advantage that they can cover large areas even across national borders and be repeated frequently at lower costs. National satellite-based forest maps with about 25 m resolution have been available in Sweden for almost two decades, and ongoing work to derive world-wide ground height

mosaics or large-scale forest height mosaics have also been presented for other regions [5,6]. Swedish mosaics based on optical satellite data from the Landsat or SPOT-5 satellites, combined through a k-nearest-neighbour (kNN) algorithm with field data from the Swedish National Forest Inventory (NFI), have been produced recurrently with a five-year interval since the year 2000 by the Swedish University of Agricultural Sciences (SLU) and the Swedish Forest Agency [7,8]. A nation-wide VOL map for the entirety of Sweden has also been generated using the BIOMASAR algorithm with Advanced Land Observing Satellite (ALOS) Phased Array type L-band Synthetic Aperture Radar (PALSAR) data from 2010 [9–11]. The kNN-based maps have required at least one cloud-free acquisition for each location of the entirety Sweden, which has been a tough requirement to achieve within a single year due to the cloudy conditions. Moreover, the mosaicking has required large efforts in order to obtain a consistent, accurate and user-friendly map. Radar-based maps have the advantage of not being dependent on cloud-free conditions. However, the BIOMASAR algorithm builds upon the backscattered radar power, and like the optical kNN-based maps, the acquisitions describe the forest in only two dimensions (2D). This causes saturation (loss of sensibility) of VOL when the canopy closes since this is dependent on the wavelength and occurs at about 100 tons/ha biomass, corresponding to  $\sim 160 \text{ m}^3/\text{ha}$  for an L-band system, and even earlier for C- and X-band systems [12,13]. A big advantage of ALS data is that they capture the forest in three dimensions (3D), hence providing forest structure such as tree height and tree density (including smaller stems covered by larger trees and hence concealed from above). The Swedish land survey (Lantmäteriet) has carried out Sweden's first full coverage of ALS data ( $0.5 \text{ points/m}^2$ ) during 2009–2016. SLU and the Swedish Forest Agency have used these ALS data to generate nation-wide maps of forest variables, similar to the earlier ones based on kNN and optical data, but with higher accuracy and with  $12.5 \text{ m}$  pixels [3]. This freely available ALS-based product has changed how forest companies cope with inventories and remote sensing data, and it has enabled small individual forest owners to obtain as good estimates of their forest stocks, as only timber buyers earlier would possess. To date, people interested in Swedish forest due to various reasons (e.g., local ecology, stored biomass, timber values, etc.) are demanding frequent updates of the published ALS-based forest maps.

The German SAR mission TanDEM-X uses two satellites (launched in 2007 and 2010) flying in close formation with the primary objective being the generation of a global digital elevation model [6,14,15]. They carry X-band SARs, and together, they constitute the first consistent flying, long-term interferometer in space, covering the entire Earth. After that, the Shuttle Radar Topography Mission demonstrated the interferometer proof-of-concept in the year 2000. Multiple research papers have demonstrated the ability of the TanDEM-X system to explain and predict forest variables, primarily AGB, VOL and tree height, in various forest types, ranging from sparse boreal forest, to tall, dense rain forest in the Amazonas [16–25]. They were mainly of two types: either model based, originating in some physical modelling of the forest, or regression based, where the variable of interest were directly dependent on the SAR observables. Yet, the current paper demonstrates the first known large-scale X-band mosaic of forest AGB/VOL, using >500 TanDEM-X acquisitions of Sweden, covering an area of  $\sim 450,000 \text{ km}^2$ , of which  $\sim 70\%$  is forest land and  $\sim 50\%$  productive forest (can produce at least  $1 \text{ m}^3/\text{ha}/\text{year}$  of wood).

The objectives of this study are to investigate requirements, possibilities, challenges and solutions to an efficient large-scale processing of TanDEM-X data, using the observables backscatter, coherence and phase height. The second objective is to evaluate the estimated accuracy from the automatically generated mosaics, in terms of root mean square error (RMSE) and bias at the stand level. The variables of interest, above-ground biomass and stem volume, are used interchangeably when methods and consequences are concerned, which is motivated in Section 2.

## 2. Material and Methods

Remote sensing data (airborne laser-based digital terrain model (DTM) and TanDEM-X data), weather data and field reference data were available to generate the AGB/VOL maps of Sweden (Figure 1). Out of the remote sensing data, three observables (explanatory variables) were derived,

denoted backscatter, phase height and coherence. These were processed scene-wise, but projected on to the nation-wide ALS DTM mosaic, which therefore facilitated the following mosaicking of the respective observable. The mosaics had overlaps, and hence, regions were overridden by observables from other neighbouring scenes. The projection order was computed from the following criteria: (1) scenes with higher temperature should be given the highest priority (be at the top of the stack), and (2) scenes with a lower height-of-ambiguity (HOA) were given precedence over those with higher HOA.

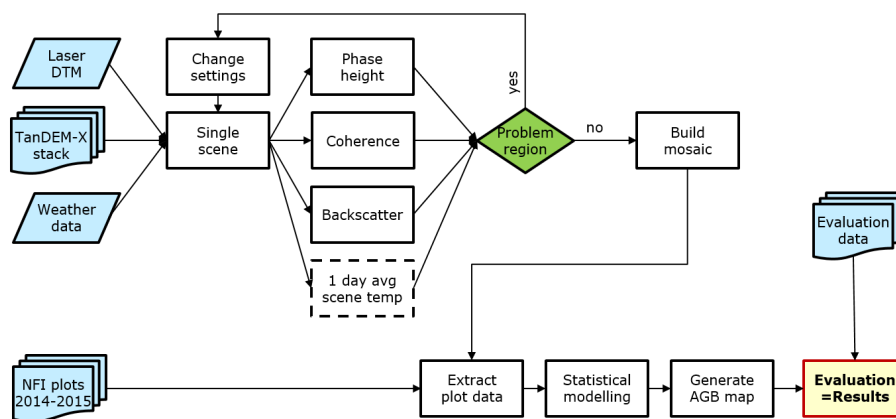


**Figure 1.** Flowchart of the working process, with material, data processing, modelling and evaluation. NFI, National Forest Inventory.

## 2.1. Material

The material used in this study covered Sweden wall-to-wall (even though field data were samples), which implied a land area of 41 million ha, of which 22 million ha were productive forest. Sweden is situated almost completely in the boreal forest region, though the southernmost parts are within the hemi-boreal and nemoral regions. About 5.2 million ha were mountainous vegetation; 5.1 million ha were wetland; and 2.9 million ha were farming land [26,27]. The forested land was dominated by Norway spruce (*Picea abies* (L.) H. Karst.), Scots pine (*Pinus sylvestris* L.) and birch (*Betula* spp.), where pine and spruce constituted about 80% of the growing stock. In the hemi-boreal and nemoral regions, there were also forests dominated by beech (*Fagus sylvatica*) and oak (*Quercus robur*) present. The current total stem volume of growing stock is 3398 million m<sup>3</sup>, and the total AGB is more than 2500 million tons. The average AGB and VOL is 58.6 tons/ha and 106 m<sup>3</sup>/ha, respectively. The forest can locally reach approximately 550 tons/ha for AGB and 1400 m<sup>3</sup>/ha for VOL, according to the Swedish NFI [27].

The material consisted of field data, TanDEM-X radar acquisitions and an external digital terrain model (DTM) from ALS provided by Lantmäteriet.

### 2.1.1. Field Data

The Swedish NFI consists of permanent (10 m radius) and temporary (7 m radius) field samples, randomly located all over Sweden [26,28]. The plots within each field sample are located in square or rectangular clusters (Figures 2 and 3). The country is divided into five strata with decreasing sampling intensity as the amount of forest decreases (typically further north and at higher altitudes). The side length of the clusters varies from 300 m in the south to 1800 m in the north, and the distance between plots within a cluster varies from 300 m in the south to 600 m in the north. Approximately 9500 sample plots belonging to 1100 clusters are field surveyed annually, and 60% are permanent plots, revisited every five years, while the remaining 40% are temporary plots that are measured only once. When non-forest plots or plots located on forest borders (transitions between forest land and non-forest land) had been removed, there were in total about 4000 field plots available per year (both

permanent and temporary), located in the forest. However, in the modelling process, the standard deviation (SD) of the AGB/VOL modelled from the temporary plots was larger compared to the permanent ones, likely because of a lower coordinate accuracy and a smaller plot size (factor of 2). Therefore, with the large amount of plots available, it was decided that only permanent plots should be used as model training data. Then, 2288 plots were available from 2016. The trees were calipered on different concentric plot sizes depending on the diameter at breast height (DBH) of the trees (Figure 2). A large number of forest variables was measured or estimated on each plot, including basal-area weighted mean tree height, basal-area weighted mean stem diameter, basal area, stand age, AGB and VOL. The plots were positioned with GPS receivers (Garmin GPSMAP 64), which have a horizontal positional accuracy of approximately 5 m, and most permanent plots had also been assigned updated coordinates using a high precision GPS receiver with a positional accuracy of 1 m [3].

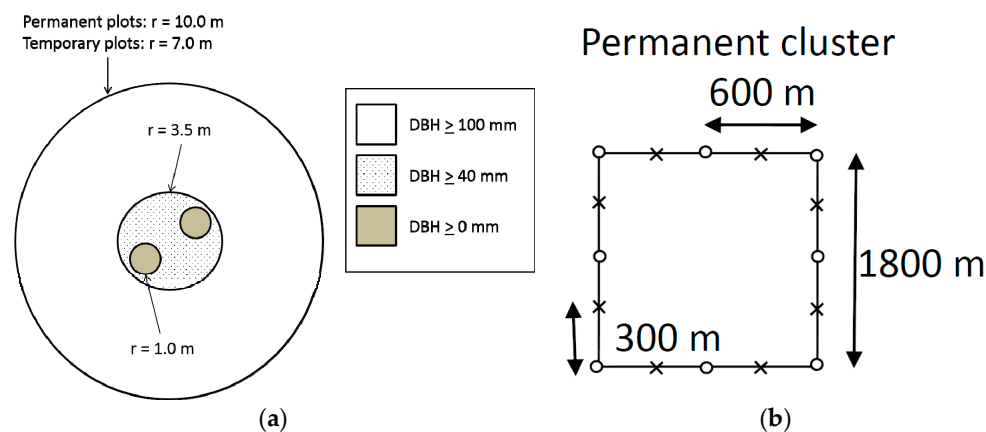


**Figure 2.** (a) Sample plot design used in the Swedish NFI since 2003. Note that trees with a diameter at breast height (DBH) of 100 mm or more are measured using different plot sizes on permanent and temporary plots. (b) Spatial arrangement of sample plots used in the Swedish NFI since 2003.

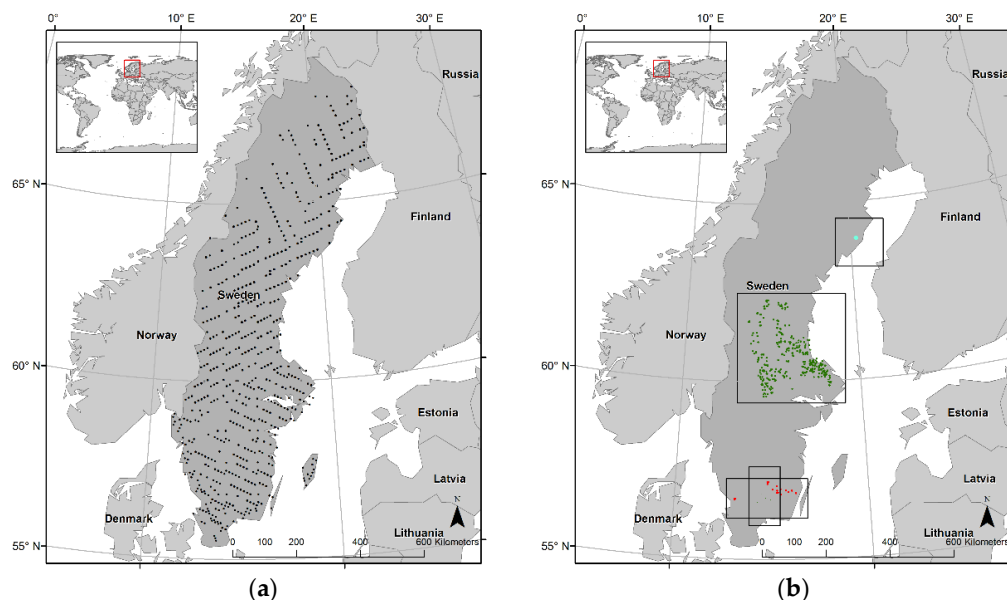


**Figure 3.** Coverage of Sweden with (a) NFI plots of 2016 used for model training and (b) evaluation stands from the three datasets. National maps© 1995–2017 ESRI.

For evaluation, three different datasets from northern, central and southern Sweden have been used (Figure 3b). The forest composition can be slightly different in the different regions with changing



altitude. The dataset from northern Sweden consisted of eleven forest stands located at Bäcksjön outside of Umeå. They were objectively inventoried by SLU in 2016 (except for one stand that was inventoried 2015), which means randomly locating about 10 sample plots that were inventoried within each stand. For small stands, fewer plots could be used. In contrast, practitioners often use subjective inventory methods, such as the relascope at subjectively chosen locations instead. All plots were inventoried with a 10 m radius. The diameter and species of all trees and the height of a subset of trees were measured to model the stand attributes (AGB and VOL) at the plot level. The subset consisted of about 10% of the trees, announced by the calliper, which randomly selected the trees, weighted by their basal area. Stand level results were calculated as the mean of the plot values. The access to all inventoried metrics enabled us to determine both AGB and VOL, using established functions [29,30].

The stands across central Sweden were forest company stands. These represent typical forest stands used as planning and operational units in forestry. In total, 354 company stands were provided. These have been objectively inventoried during 2015 using 3–14 circular sample plots randomly located within each stand. The plots were typically of an 8 m radius, but could range between a 5 m and a 10 m radius, and the amount of plots and the radius varied depending on the size and heterogeneity of the stand. The diameter of all trees and the height of a subset of trees (as in northern Sweden) were measured to model the stand attributes at the plot level, and stand level means were calculated. The VOL was determined using functions from [29], but no AGB was computed, as only the processed data (with VOL) were provided by the company. The sampling error was expected to be small, and the accuracy of this inventory method was further presented and discussed in [31].

The dataset from southern Sweden consisted of ten stands sampled with 10 randomly-located sample plots with a 10 m radius, inventoried in 2016, and eight stands with 4 randomly-located sample plots with a 10 m radius, inventoried in 2017. Only DBH was measured on these sample plots. AGB and VOL were determined with the same set of functions as described above, but without using heights. The attributes for the training and evaluation datasets are presented in Table 1.

**Table 1.** Forest attributes for the field datasets. *n* denotes the number of stands or plots, and standard deviation is denoted as SD.

Dataset	Purpose	Forest Attribute	Mean	Min	Max	SD	Unit	<i>n</i>
Swedish NFI	Training	AGB	86	0	369	59.3	tons/ha	2288
Swedish NFI	Training	VOL	162	0	874	129	m <sup>3</sup> /ha	2288
Northern Sweden	Evaluation	AGB	117	36	218	63.0	tons/ha	11
Northern Sweden	Evaluation	VOL	219	56	395	120	m <sup>3</sup> /ha	11
Central Sweden	Evaluation	VOL	203	0	577	102	m <sup>3</sup> /ha	354
Southern Sweden	Evaluation	AGB	152	38	339	86.0	tons/ha	18
Southern Sweden	Evaluation	VOL	286	49	657	170	m <sup>3</sup> /ha	18

The correlation between AGB and VOL was strong for all datasets where both variables were available ( $r = 0.983$  for the averages from the 2288 NFI plots,  $r = 0.996$  for the evaluation stands in northern Sweden and  $r = 0.995$  for the stands in southern Sweden). The conversion factor between VOL and AGB was 0.54, 0.53 and 0.52, respectively. They have long been used interchangeably, and AGB is typically related to VOL through a constant of about 0.6 [4]. This implies that both AGB and VOL are considered when effects and reasons are mentioned throughout the article, despite only VOL being available for some of the reference data.

### 2.1.2. Remote Sensing Data

There were 518 TanDEM-X acquisitions collected over Sweden from 2 October 2015–31 January 2016 (Figure 4a). This corresponded to Swedish fall and winter conditions, and the acquired air temperatures registered from weather stations close to the scene centres ranged from  $-32$  °C to  $+11$  °C. There was no opportunity to decide the acquisition dates, since the satellite mission is used for multiple purposes,

and interferometric SAR (InSAR) requires certain acquisition geometries to work. The images were acquired in strip-map mode with the HH polarization (horizontally transmit, horizontally receive). Since single polarization is the standard mode for the global mapping, there was no opportunity to choose another polarization. The HOA were in the range 55–65 m for all acquisitions except the first three passes, where the HOA was in the range 24–32 m (hereafter denoted as low height-of-ambiguity; Figure 4a). In northern Sweden, a small stripe was not covered in any of the passes. The mean scene incidence angles were all in the range of 38°–45°.

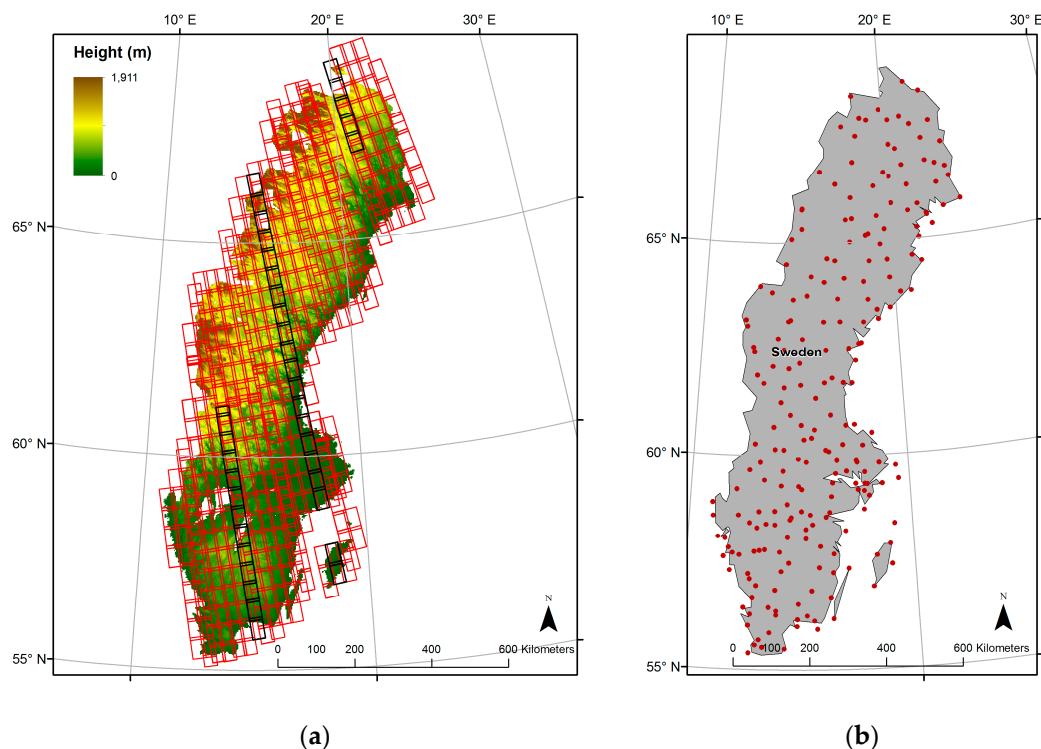


**Figure 4.** (a) Illustration of the TanDEM-X coverage of Sweden with the three stripes of low height-of-ambiguity highlighted in black. The scenes are overlaying an ALS DTM to illustrate the structure of the landscape. (b) The available weather stations from which temperature data were collected. National map© 1995–2017 Esri.

The DTM utilized was produced by Lantmäteriet from ALS data, with a  $0.5\text{-m}^{-2}$  point density and rasterized with a 2 m pixel size [32,33]. All data were handled in the SWEREF99TM coordinate system. However, maps presented at large scales are illustrated in Lat. Lon. WGS84 in this article.

### 2.1.3. Metrological Data

A network of 226 weather stations (Figure 4b) is distributed across Sweden by the Swedish Meteorological and Hydrological Institute (SMHI). From these stations, the daily average temperature was available. For each scene, the station with the shortest distance from the scene centre was selected, and the average temperature for the date of acquisition was obtained. The use of precipitation data was also considered, but ignored, since earlier experiences and other studies have indicated that precipitation does not greatly influence the InSAR observables at X-band [34].

### 2.2. Field Data Processing

In order to achieve as robust and correct models as possible, and with the access to thousands of NFI plots, the NFI plots were filtered. This included removal of zero-phase-height plots and removal of NFI plots with a mean AGB < 10 tons/ha.

### 2.3. SAR Data Processing

The TanDEM-X data were delivered in coregistered single-look slant range complex (CoSSC) format, and the processing was performed using the software Gamma (Gamma Remote Sensing AG) [35]. An advantage of TanDEM-X data acquired as interferometric pairs (consisting of one image  $s_i$  from each satellite  $i$ ) implied that the backscattering coefficient ( $\sigma^\circ$ ) could be computed from each acquisition pair, as well as the coherence ( $\gamma$ ) and the interferometric phase ( $\varphi$ ). The single-look complex (SLC) data from respective satellite were multilooked with a constant factor of 5 by 5 looks. The SLC resolution was 2.5 m in slant range and 3.3 m in azimuth (with a pixel spacing of 1.36 m and 1.84 m, respectively), and the processed  $\sigma^\circ$ ,  $\gamma$  and  $\varphi$  rasters were finally resampled onto the ALS DTM grid with 10 m  $\times$  10 m pixels. The geocoding was carried out using a lookup table, generated by using the cross-correlation between a multilooked intensity image from one of the satellites and a simulated SAR intensity image, which could be created from the ALS DTM and the satellites' orbit data [36].

#### 2.3.1. Computation of Backscatter Raster

The calibration gain provided in the metadata for each acquisition (about 50 dB) was subtracted from the multilooked intensity images ( $\beta^0$ ), before a radiometric normalization based on the pixel-area method was applied, as described in [37,38]. One backscatter image  $\sigma^\circ$  per acquisition pair was then computed as the arithmetic mean of the two normalized backscatter images within the image pair.

#### 2.3.2. Interferometric Phase Height

A complex interferogram is computed as the Hermitian product of two complex images  $s_1$  and  $s_2$ , using coherent multilooking. The corresponding InSAR observable, the complex correlation coefficient  $\tilde{\gamma}$ , was therefore estimated as [39–41]:

$$\tilde{\gamma} = \frac{E[s_1 s_2^*]}{\sqrt{E[|s_1|^2] E[|s_2|^2]}} \quad (1)$$

where  $E[\cdot]$  denotes the expectation value and  $*$  the complex conjugate. To reduce phase noise, the interferogram was derived with a spatial averaging of 5 looks in range and 5 looks in azimuth. This reduced the phase noise standard deviation by approximately a factor of 5 [42]. The interferogram was flattened by subtracting the ground phase, derived from the satellite orbit data and the ALS DTM. The estimation of the ground phase was not always correct, and often, a phase trend of several radians was introduced across the scene. This is further discussed in Section 2.4.2. The flattened interferogram was adaptively filtered with a function based on the local fringe spectrum and using a coherence kernel of 3  $\times$  3 pixels and a 16-pixel fast Fourier transform window [43]. The filtered output was then masked from water bodies (described in Section 2.3.4) before applying a minimum cost flow phase unwrapping algorithm [44] to unwrap the phase. The quality of the unwrapped phase was enhanced by selecting a suitable starting location with as high coherence as possible, which was obtained by sampling coherent spots in the coherence image every 10th line and every 10th row, also computed from the images  $s_1$  and  $s_2$ . The unwrapped phase was converted to height using a phase-to-height sensitivity raster, which was generated from the differential interferometric phase and the orbital state vectors, using Gamma. The phase height raster was filtered to the range [−4, 35] m since we do not expect any heights to extend beyond the highest Swedish trees (35 m), nor should they possibly become negative. The phase height was typically below 20 m, and the kind of large negative acceptance was selected based on the histogram of phase heights, which did not show a significant drop at 0, but rather at several meters below. When visually inspecting the phase height raster and statistically evaluating models relating to AGB/VOL, it became clear that a lot of information was lost if a strict height limit of 0 were applied.

### 2.3.3. Computation of Coherence

The coherence  $\gamma$  was estimated from the normalized interferogram and the multilooked intensity images, using a coherence window of  $3 \times 3$  pixels as described in:

$$\gamma = \frac{|\sum_i s_{1,i} s_{2,i}^*|}{\sqrt{\sum_i |s_{1,i}|^2 \sum_i |s_{2,i}|^2}} \quad (2)$$

where subscript  $i$  denotes pixel  $i$ . However, the coherence was prominently attenuated against the scene sides (in the range direction). For the global coverage of TanDEM-X data, two full Earth coverages were produced. The second coverage was shifted by half the beam width of the first acquisition. This ensured that regions with lower antenna gain at the edges of the main lobe from the first coverage were covered with a higher antenna gain at the other acquisition. To keep the gain in the main lobe as high as possible, the beams were not amplitude tapered to flatten them. This caused the acquisitions over Sweden that were only acquired once to drop antenna gain up to 3.3 dB at the edges. Amplitude tapering is used to flatten and broaden the near beams to obtain sufficient performance over the whole swath [45]. In order to compensate for the antenna gain loss and make use of the coherence at any location, a correction was computed scene-wise as described in [46] and illustrated in Figure 5. In short, it consists of two parts. First was a coherence compensation due to the decreasing signal-to-noise ratio (SNR) at the scene sides, which can be calculated as the noise floor information, which was provided as a polynomial of degree seven in the slant range, in the metadata. Second was a compensation due to any residual processing errors, which was applied to all pixels. The finite scene side sensitivity of the SAR system can be modelled as the coherence loss, defined by [47,48]:

$$\gamma_{SNR} = \frac{1}{\sqrt{1 + SNR_{TDX}^{-1}} \sqrt{1 + SNR_{TSX}^{-1}}} \quad (3)$$

where  $SNR_{TSX,TDX}$  is the signal-to-noise ratio of the two satellites. The SNR is a measure that describes the quality of the SAR system, estimating how much the radar signal has been corrupted by noise. It depends on the backscattered power  $\beta^0(R, z)$  and the noise equivalent backscatter  $\beta_{ne}^0$ , which was estimated and provided in the TanDEM-X metadata (Figure 6). Residual processing errors could be detected when the coherence cumulative density for raw coherence was inspected, as it did not approach the expected unity, but rather a value  $\gamma_P$  below. Hence, the estimated coherence was divided by this constant  $\gamma_P$ , and any coherence pixels hereafter exceeding one were set to unity. Figure 6 illustrates an example of (a) the SNR correction polynomial and (b) the cumulative coherence distribution before and after correction. The compensations varied with the scenes, but the noise floor was typically  $-22$  to  $-26$  dB; and the residual constant  $\gamma_P$  would typically take values of about 0.95, but for some scenes, it even reached as low as 0.85. The coherence with these corrections applied will hereafter be denoted as corrected coherence.

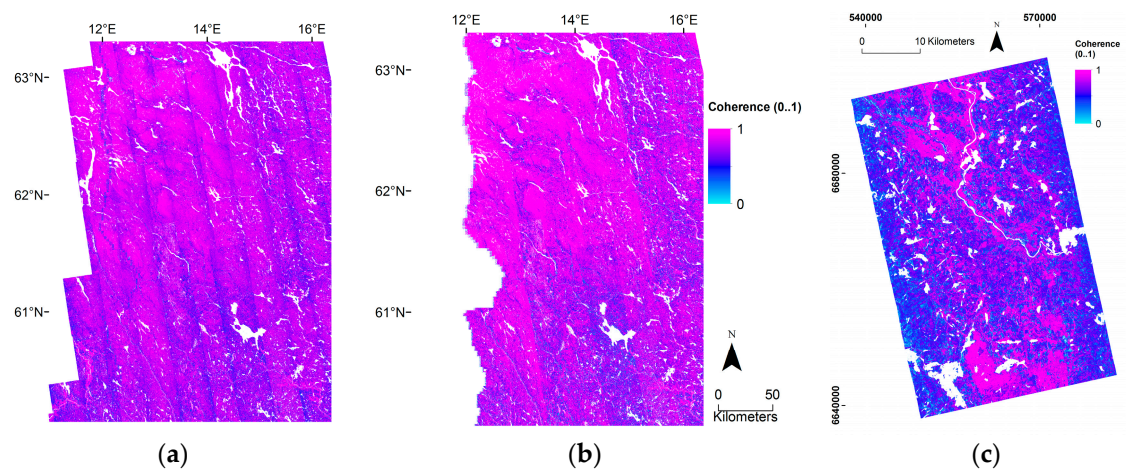


**Figure 5.** Illustration of the differences in coherence between different satellite orbits and within single scenes before (a) and after (b) correction. An enlarged example of the range-wise attenuation within a single scene is demonstrated in (c).

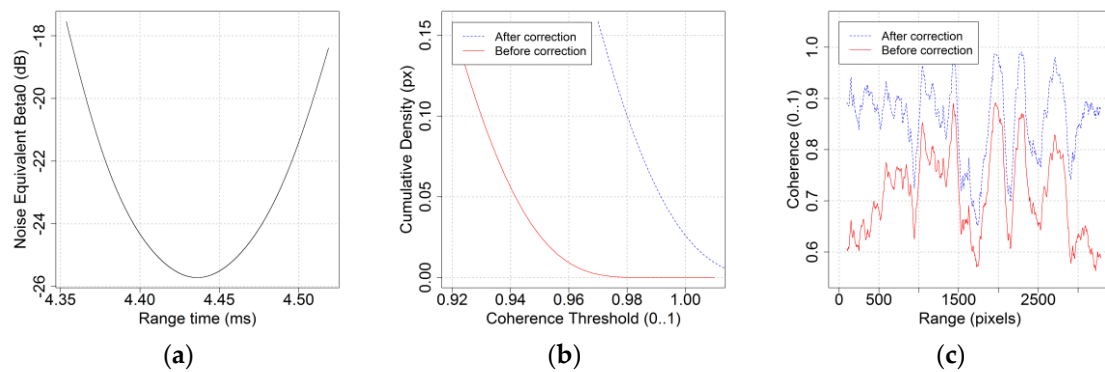


**Figure 6.** An example of (a) the noise floor polynomial, (b) the cumulative coherence distribution before and after residual error correction and (c) a range cut of the coherence across a November 2015 image.

#### 2.3.4. Derivation of Water Mask

A water mask was computed using the two intensity images and the coherence image. Fixed thresholds of 0.2 for coherence and 0.25 for the normalized intensity were used to define water bodies. The values were selected by trial-and-error to get a reasonable output. In addition to this, heights below 0.7 m altitude were defined as water. The sea-level restriction was helpful to avoid noisy conditions in the archipelago, which otherwise influenced the phase trend corrections greatly (described further in Sections 2.4.1 and 2.4.2).

#### 2.3.5. Geo-Location

The geocoding was carried out scene-wise as described in Section 2.3, and therefore, the geolocation differs from scene to scene. The refinement of the geocoding lookup table was repeated twice, to make sure the current algorithm converged [36]. Despite this careful and robust geocoding, geolocation errors were impacting the end product greatly. The inherent nature of side-looking radar systems causes shifts at forest borders and hilly terrain. Hence, the impact of geolocation errors can be rather large for smaller stands or at the plot level (as is the case for the model training), in the case of heterogeneous forest, while these problems usually decreases with larger stands and higher



homogeneity. In Figure 7, a number of examples on the current geolocational accuracy of TanDEM-X phase heights is compared to Lorey's height estimated from ALS data.

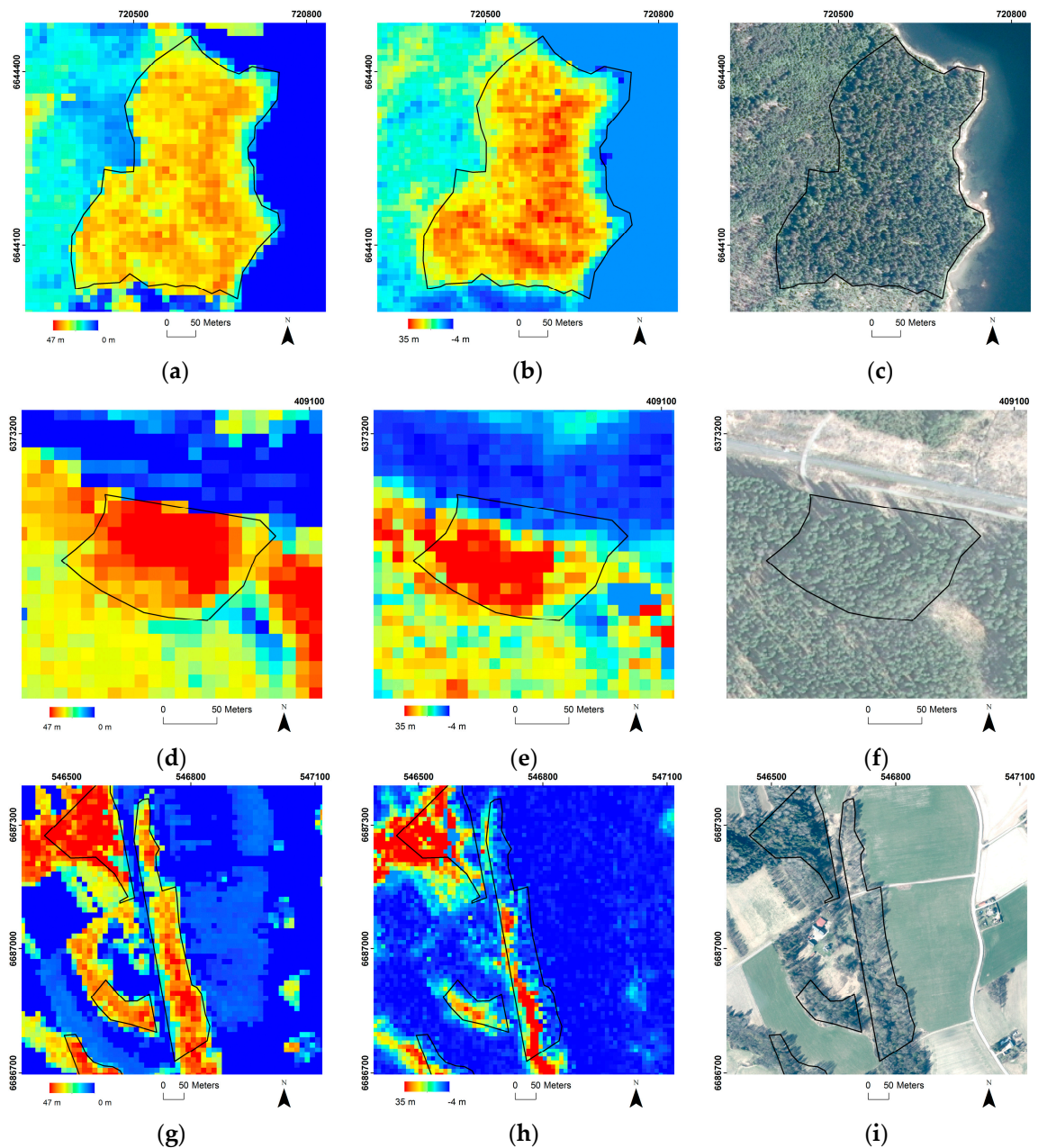


**Figure 7.** Examples on the geolocation accuracy. First column (a,d,g), Lorey's height estimated from ALS data; second column (b,e,h), TanDEM-X phase heights; and third column (c,f,i), ortho photographs from Lantmäteriet<sup>®</sup>.

In Figure 7a–c, a quite large stand (10.5 ha) is illustrated, where the pixels of erroneous geolocation along the eastern border do not greatly influence the overall stand estimate. In Figure 7d–f, a much smaller stand is described, with a geolocation error of about 2 pixels in the north–south direction. Because of the smaller stand size, 1.5 ha, and no forest at all in the wrongly-mapped pixels, the influence of the stand estimate becomes larger. In Figure 7g–i, the long central stand is 9 ha large, but the shape of it and the several pixel errors along the eastern side cause a large stand estimated error.

## 2.4. Special Processing Cases

### 2.4.1. Scenes with Too Low HOA for Forest Mapping

Three orbits (2, 5 and 6 October 2015), which were the first three satellite passes during the Swedish acquisition period October 2015–January 2016, acquired images with an HOA in the range of 24 m–32 m. This gave a very high sensitivity for small height changes, but also had the effect of causing ambiguities (Figure 8) for the phase unwrapping, as the trees in the forest were within the same range. The falsely unwrapped pixels could be post-processed by folding phase multiples of  $\pm 2\pi$  into the  $0-2\pi$  region, starting with the pixels furthest away, and iteratively shift inwards to approach the  $0-2\pi$  region. This was performed using a fixed thresholding of pixels exceeding multiples of  $2\pi$  across the image, which required the phase to be only the residual phase above the DTM. However, the flattening of the phase using the simulated DTM phase was not always accurate and introduced a trend (described in Section 2.4.2), which made it impossible to implement a robust unfolding of falsely-unwrapped phases for these low HOA acquisitions. The phase jumps could appear wherever the unwrapping algorithm found the lowest cost to be, and hence, the trend could not easily be corrected before the unfolding first was done. It was hence decided, that these scenes with low HOAs were ignored in the generation of the Swedish mosaic.

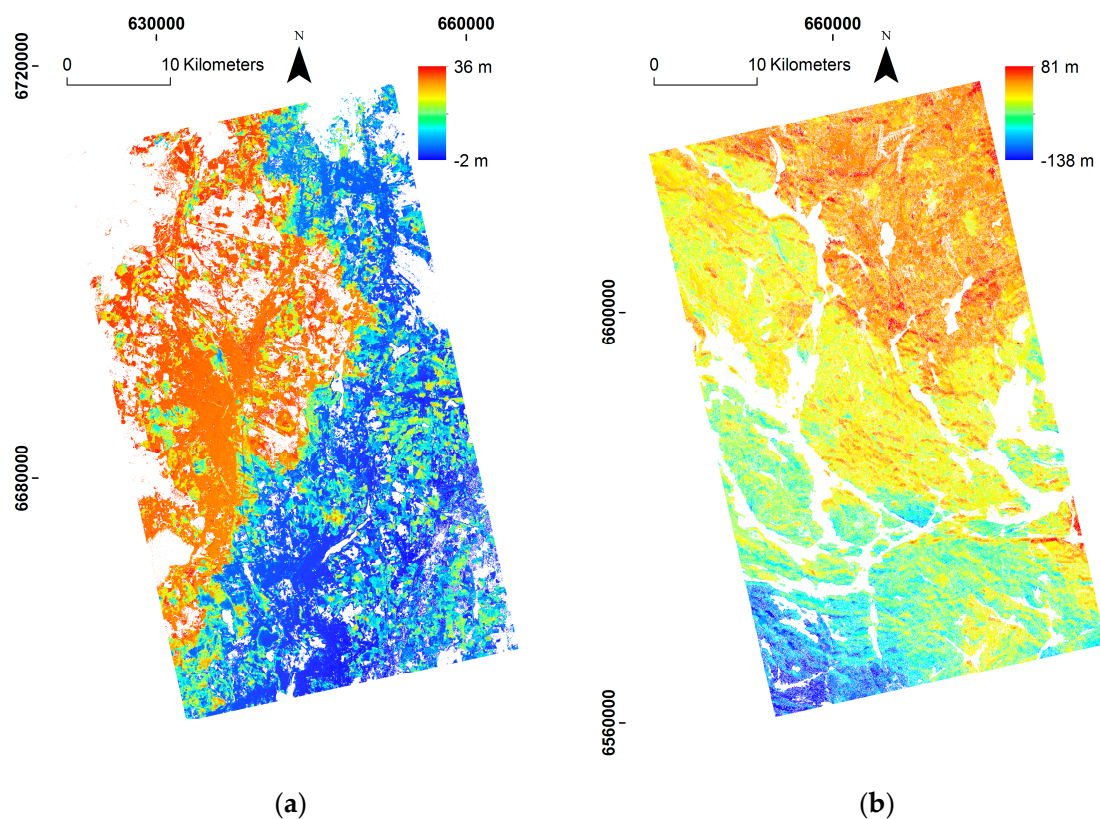


**Figure 8.** Two examples of falsely-unwrapped phase heights, with (a) half of the image having been assigned entirely wrong heights, as these phases (or the cost of unwrapping them) exceeded the allowed range  $[-\pi, \pi]$ , normally constraining heights to lie within the valid height of ambiguity (HOA), and (b) in addition to large regions being wrongly unwrapped, also large spots of incorrect heights are interspersed within the wrong regions, e.g., the red spots within the yellow central region possess heights that are at least HOA m larger than the yellow heights.

#### 2.4.2. Scenes with Phase Trends

During the data processing, the ground phase was simulated from the ALS DTM based on the metadata information of the satellite position. The ground phase was subtracted from the phase height in order to obtain the phase height above the ground surface. A residual phase trend, sometimes changing up to 30 m across the swath, was introduced (Figure 9). The residual phase trend is caused by small errors in the satellite positions, which result in baseline errors. Similar trends have been reported by other authors [6,15,16,21,49]. The error is easily observed in overlapping areas between adjacent swaths and can be corrected, to first order, by fitting an error model to the data. Hence, to date, one solution to handle this was to fit a two-dimensional polynomial in the regions corresponding to open ground, in the form of  $correction = \alpha_0 + \alpha_1 \cdot az + \alpha_2 \cdot rg$  to the scene, where  $\alpha_i$  with  $i \in (0, 2)$ , described the coefficients for the pixel number in the azimuth ( $az$ ) and range ( $rg$ ) directions (Figure 9c), a solution that was used also in other studies [16,21]. In these open regions, the ALS DTM should coincide with the registered phase height, and hence, a reasonable correction could be found. Still, a large difficulty was automatically defining which regions contained no forest. This was done by defining a non-forest mask based on the coherence, as the coherence tended to be higher for open regions compared to forested regions and lower for water bodies and denser forest. However, a large portion of overlap occurred between the regions (Figure 10a). Since the coherence varied from acquisition to acquisition due to weather conditions, ground temperature (with frozen conditions, the coherence increased and the range of coherence decreased drastically) and possibly more reasons, a relative threshold was applied [50,51].

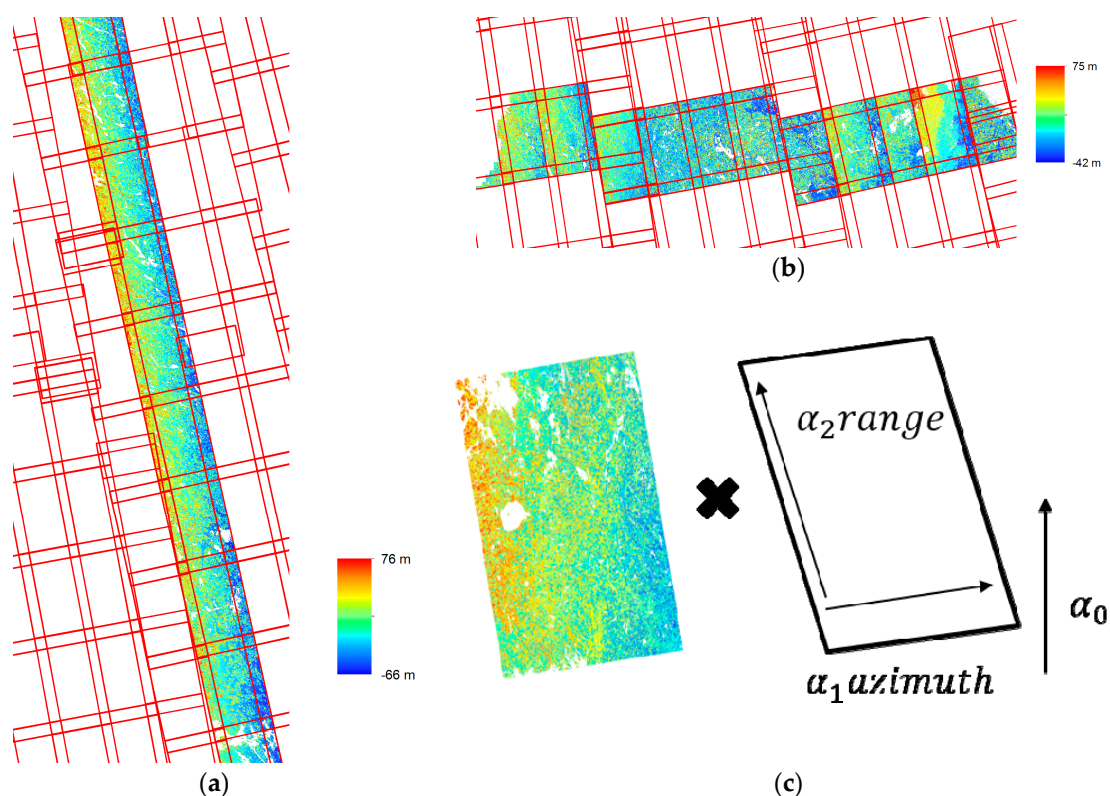


**Figure 9.** Illustration of the phase trend appearance in images with merely the unwrapped phase for (a) an along track orbit and (b) acquisitions from several track orbits. (c) Illustration of how a single scene was multiplied with a correction raster, based on the coefficients  $\alpha_{0,1,2}$ .

The reference coherence was defined as the scene average coherence, after the water mask was applied. Then, an “open ground” coherence mask was defined as coherence pixels in the range of 105%–120% of the reference coherence. From the filtered open ground, the two-dimensional polynomial



was fitted and subtracted from the entire raster. This was still not a sufficiently robust solution for all scenes, so to gain a better result, this polynomial fitting was carried out on strongly multilooked SLC images with a factor of  $80 \times 80$  pixels, but the correction was applied to the full resolution images ( $5 \times 5$  pixels multilooking). This was sufficient for most images, but when examining the result closely, the phase of open ground still generally possessed slightly negative heights. However, since the phase height was now approximately correct, and more stable compared to the coherence, a new “open ground” mask was defined with the stricter coherence limits of 115%–128% relative to the reference coherence and used concurrently with the range of the phase height within  $-10$  to  $0$  m. The polynomial fitting and correction were hereafter repeated, this time at the full resolution. The reason to not use only a lower limit, and go all the way up to unity, was that unwanted objects were also included among the high coherence pixels, especially in regions with many solid objects (e.g., buildings). For such pixels, the coherence was close to 1, while the phase height was tens of meters. Hence, if these pixels were included when the polynomial was fitted, it would imply a strong downwards shift, causing, again, too low phase heights. However, when the collected mosaicked phase height (now with the experience of being correctly adjusted) was plotted against the VOL for the 2288 NFI plots (Figure 10b), the phase height approached  $-2$  m as the VOL approached  $0 \text{ m}^3/\text{ha}$ . Hence, an upward shift of  $2$  m was added to the phase height mosaic, to obtain an empirical model established from a physical reasoning (where neither the phase height, nor the AGB/VOL should be negative). This also enabled the use of a zero intercept model (Section 2.4.4).

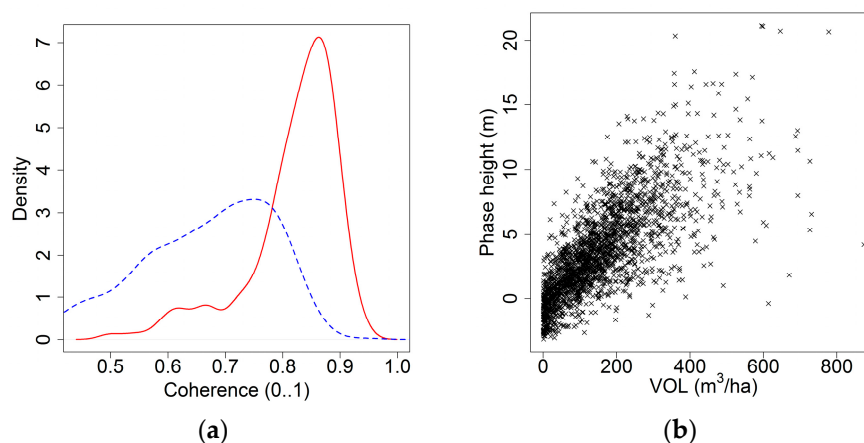


**Figure 10.** (a) Plot density of the NFI plots with regard to the coherence  $\gamma$ . Forest ( $>80$  tons/ha, dashed blue) and open ground ( $<10$  tons/ha; solid red). (b) Scatter plot of uncorrected phase height against VOL.

#### 2.4.3. Scenes Acquired in Frozen Conditions

The ground conditions varied with the air temperatures ranging from  $-32$  °C to  $11.3$  °C. Although the temperature alone does not fully explain the changes of the SAR interaction in the forest compared to summer conditions, some tendencies became noticeable. Generally, the phase height decreased in frozen conditions, mainly due to less water content in the trees and a reduced dielectric constant. However, some scenes acquired in October had just reached the first days with temperatures around zero, and here, the phase height decrease was less prominent, and likewise, for a few scenes acquired in January 2016 with a longer time of low temperatures far below  $0$  °C, the phase height remained lower despite the temperature being around  $0$  °C or thawing at the time for the acquisition. A limited amount of stands located in frozen conditions were used for the evaluation. Still, it can clearly be seen in the mosaic (Figure 11a) how the phase height drops in scenes with negative temperatures, especially in the northern parts of Sweden.

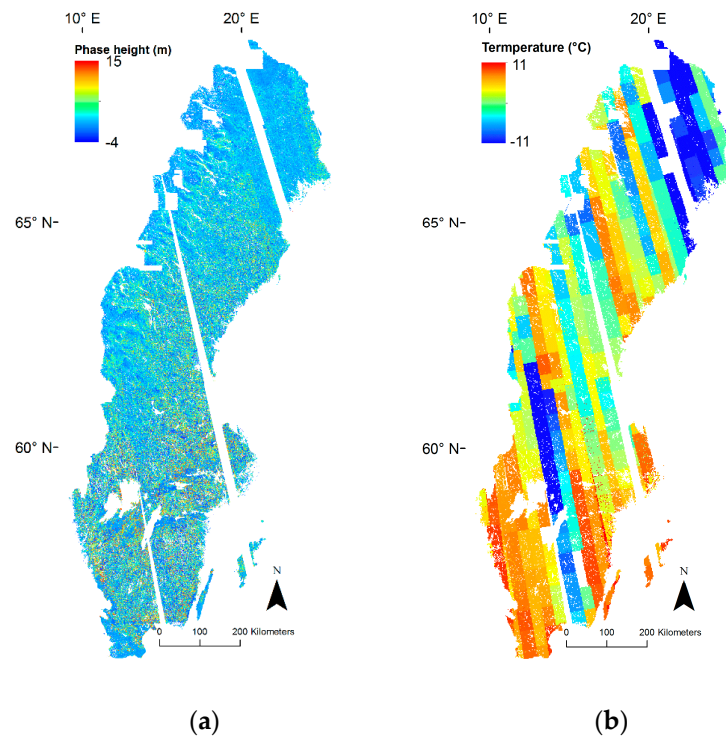


**Figure 11.** (a) Phase height mosaic. (b) Average ground scene temperatures.

#### 2.4.4. Scenes with Frozen Water Bodies

The winter conditions that were present for some acquisitions made it awkward to derive a water mask only from the coherence and backscatter, as was done for most other scenes with unfrozen sea. As can be seen in Figure 12, the backscatter and coherence took on a range of values, from very low to high, depending on the ice conditions, despite everything without a phase height representing a water body (the open sea). In the top left, the mainland is present, and the island Holmön is located in the centre of Figure 12. The thickest ice is furthest northwest and further south and east, and thinner and thinner ice (frozen at different occasions) represents lower backscatter and lower coherence. In the southeast corner, the open unfrozen sea can be seen. To filter out the sea for such scenes, the water mask criteria were applied, which defined anything below 0.7 m above the sea level as water (Section 2.3.4). Unfortunately, the lakes in the inland could not be filtered similarly. However, these rarely caused any problems when the phase trend was corrected, as they usually were homogeneously frozen and in combination with a stable phase height, they behaved similarly as flat open fields. Yet, an external water mask would be required for end user products.



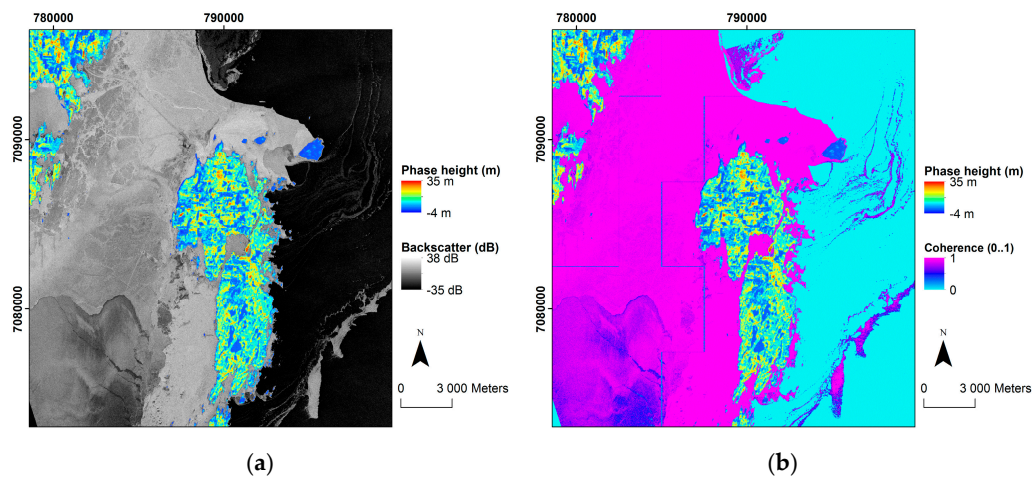


**Figure 12.** Phase height overlaying (a) the backscatter and (b) the coherence for a scene in the archipelago outside Umeå in northern Sweden, where the frozen conditions influence the options for using coherence and backscatter to filter out water bodies. The perpendicular lines are processing artefacts originating from the ALS DTM, but since all the water within 0.7 m above the sea-level was filtered away, these areas did not influence any computations.

#### 2.4.5. Scenes in the Archipelago

The wrapped phase became unwrapped by applying the water mask (which set the water bodies to NA (“not available”) values) and fed the outcome to the minimum cost flow algorithm, which was generally robust and delivered unwrapped phases of high quality. In the archipelago (which for Sweden corresponds to a 3200 km coastline), single islands were recurrently incorrectly unwrapped, with phase jumps on the order of  $\pm n \cdot 2\pi$ ,  $n$  being a positive integer. When the following trend correction was applied, the trend correction polynomial was fit to incorrect coefficients (often large), causing the resulting usually small trend corrections to actually introduce large errors with phase heights like Figure 13a. A robust way of overcoming this was to assign the water bodies a height of 0.1 m (defining 0 as NA), which stabilized the otherwise very noisy phase, and also linked the actual height between the islands, with the result as in Figure 13b).

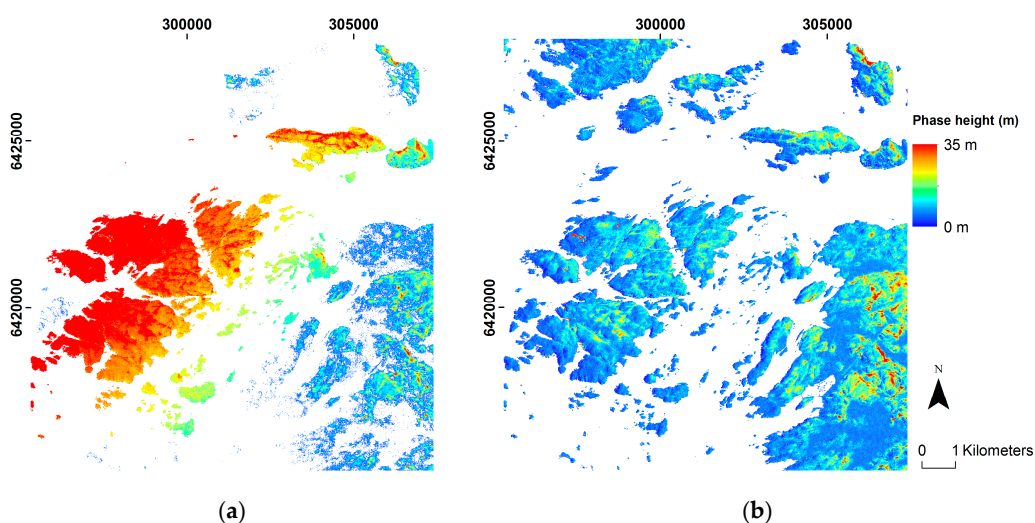


**Figure 13.** (a) Phase trends caused by incorrect trend corrections, caused by incorrect minimum cost flow phase unwrapping. Phase jumps between islands gave height differences of multiples times the HOA. (b) The same coastal region correctly unwrapped.

## 2.5. Data Extraction

From the centre coordinates for the respective permanent NFI plot, the circular surrounding was extracted from each observable raster and refined to plot average and standard deviation. The radius of 10 m would be technically correct to use, but with the pixel size of 10 m and geolocal errors of about 1–2 pixels, sometimes being as large as 3–4 pixels, larger radii (10, 20 and 40 m) were also evaluated. With the overall better correspondence with the field plot data (lower standard error) and decreased variance as the larger radii were evaluated, it was determined that a 40 m radius was more robust to use, despite the smaller sample radius. This also agrees with the findings in [16].

## 2.6. Relation between Observables and AGB and VOL

Out of the extracted data and the reference data, the backscatter did not show any stronger correlation with the VOL (Figure 14). The phase height showed a rather strong linear relation, while the coherence appeared to follow a non-linear relation to VOL. The phase height might experience a decreased sensitivity or slight saturation at volumes above 400 m<sup>3</sup>/ha. The coherence spread was large and might be due to the large amount of different acquisitions, covering many forest types and possessing different acquisition geometries. Different coherence models with a smaller spread have been explored and discussed by, for example, [23,24]. They investigated coherence models for hemi-boreal forest, but common for those studies is that they investigated one or two single test sites.

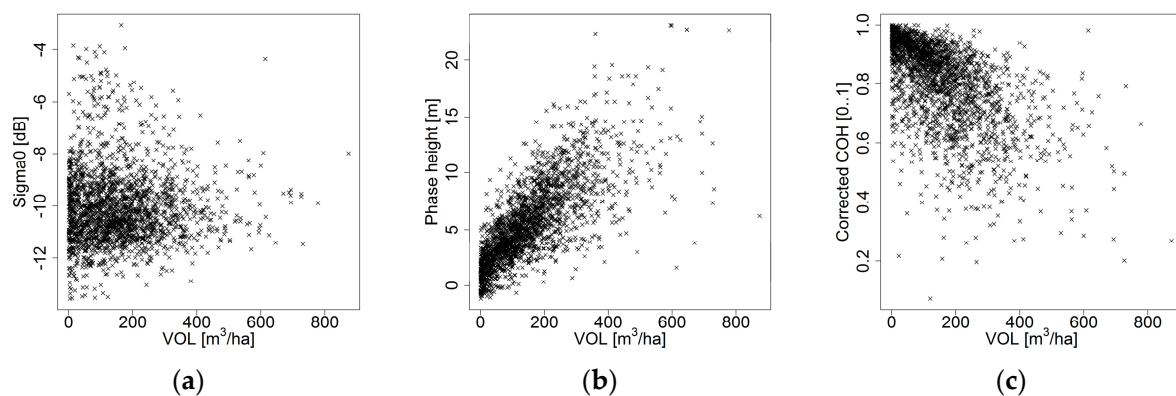


**Figure 14.** Relation between the observables (a) backscatter ( $\sigma^0$ ), (b) phase height ( $\varphi$ ) and (c) corrected coherence ( $\gamma$ ) vs. the VOL.

### 2.6.1. Observables' Dependence on HOA

The extracted observables at the NFI plot locations were plotted against the HOA, in order to detect any dependencies (Figure 15). The phase height appeared relatively similar within the available HOA range, while the range of coherences tended to decrease with increased HOA. This indicated that the coherence should be normalized with respect to the HOA for the acquisition, in order to be used correctly in a mosaic consisting of scenes with varying HOA. Yet, a useful normalization could not be found that improved the estimation of AGB/VOL.

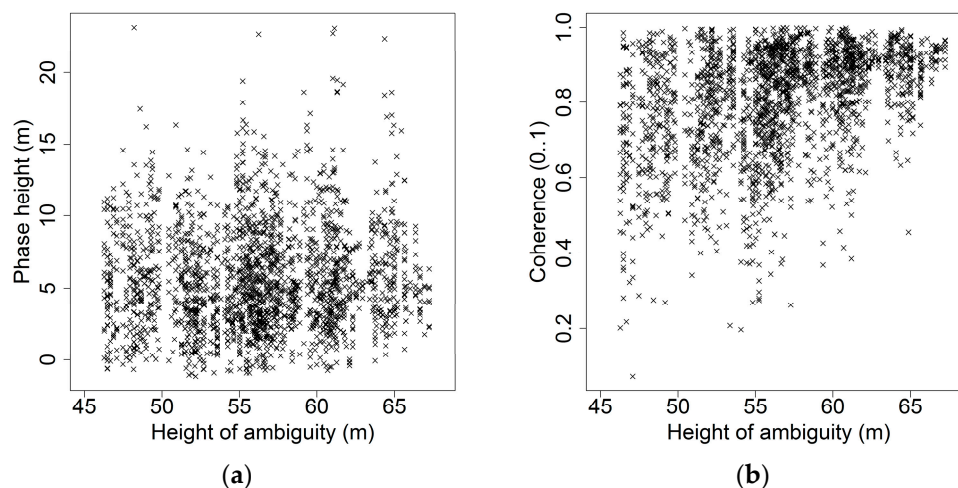


**Figure 15.** (a) Phase height ( $\phi$ ) vs. HOA. (b) Corrected coherence ( $\gamma$ ) vs. HOA.

### 2.6.2. Empirical Modelling

The observables were tested in multiple regression models. In traditional linear regression models, individual observations that do not follow the assumed modelled relationship (causing, e.g., non-normally distributed residuals) do greatly influence the fitted model, since the squared residuals are minimized. If a limited amount of observations is available, each observation that behaves differently should be manually inspected to possibly adjust the model, but in the current study, the large amount of observations combined with numerous possible reasons for deviations made this approach unsuitable. The large amount of available field data, many scenes and large spread made it convenient to use robust linear regression (rlm), available from the MASS package in the Comprehensive R Archive Network (CRAN) [52]. rlm fits models using a number of different  $M$ -estimators (estimates  $\beta$ ), compared to the more commonly-used least squares. In general, the  $M$ -estimator for a regression coefficient  $\beta$  minimizes:

$$\sum_{i=1}^n \rho \left( \frac{y_i - \sum_{j=0}^p x_{ij} \beta_j}{\sigma} \right), \quad (4)$$

as a function of  $\beta$ , where  $y_i$  is the  $i$ -th response,  $x_{ij}$  is the  $i$ -th predictor for the  $j$ -th parameter,  $n$  is the number of plots,  $p$  is the total number of parameters and  $\sigma$  is a scale parameter [53]. If  $\rho$  is differentiable, the  $M$ -estimator is said to be of  $\psi$ -type, with  $\psi = \dot{\rho}$  being the differentiation of  $\rho$ . Let  $r_i = y_i - x_i \beta$  denote the residuals, then least-squares is a special case of this where:

$$\psi(r_i) = r_i. \quad (5)$$

For the data used in this study, it was found that the loss function, Tukey's bisquare, was a good compromise between stability and minimizing the RMSE. It is defined as:

$$\psi(r_i) = \begin{cases} r_i \left\{ 1 - \left( \frac{r_i}{k} \right)^2 \right\}^2 & \text{if } |r_i| \leq k \\ 0 & \text{if } |r_i| > k \end{cases}, \quad (6)$$

using  $k = 4.685$ , which provides an asymptotic efficiency 95% that of linear regression for the normal distribution, with respect to the residuals. For small residuals, both the least-squares and Tukey's bisquare loss functions are linear, while for larger residuals, the Tukey function sets the weightings to zero.

Both models with and without intercept were tested. Models with intercept bear the risk of not gaining sufficient acceptance from a user perspective, as they indicate a certain AGB/VOL also

where there is none, because of the positive intercept. However, they were still slightly more accurate, compared to models without an intercept (in terms of lower standard error (SE), which in the robust regression case corresponds to the scale estimate). It was decided to use the model without intercept, in order to get a consistent map ranging continuously from zero and higher, and being established by a physical reasoning. By evaluating the residuals versus fitted plots, the general relation between AGB/VOL and each explanatory variable, or any transformed versions, was established. The model hypothesis was that all observables would contribute to an improved model. Although both the phase height and the coherence were significant explanatory variables, the coherence did not improve the model accuracy, when evaluated on the independent datasets. Based on these observations, the simple and yet efficient models (Equations (7) and (8)) were determined.

$$\text{AGB} = 13.5 \Phi \quad (7)$$

$$\text{VOL} = 25.2 \Phi \quad (8)$$

The model statistics are presented in Table 2. The calculation of RMSE is described in Section 2.4.4, but for the model estimation step, the residuals were computed using the leave-one-out cross-validation (cv) method, where for each  $i$ , the model was fitted from all but one observation  $i$  and then applied to observation  $i$ . The lower SEs compared to the  $\text{RMSE}^{\text{cv}}$ s can be seen as the improvements achieved by applying the robust regression compared to traditional regression.

**Table 2.** Model estimation statistics including results from residual modelling errors SE and leave-one-out cross-validation  $\text{RMSE}^{\text{cv}}$ .  $n$  denotes the number of plots.

Forest Attribute	SE	Bias	$\text{RMSE}^{\text{cv}}$	$\text{RMSE}^{\text{cv}}\%$	Unit	$n$
AGB	31.7	8.82	43.1	50.5	tons/ha	2,108
VOL	58.6	15.6	87.1	54.9	m <sup>3</sup> /ha	2,108

The distribution of reference VOLs vs. the distribution of estimated VOLs is shown in Figure 16.

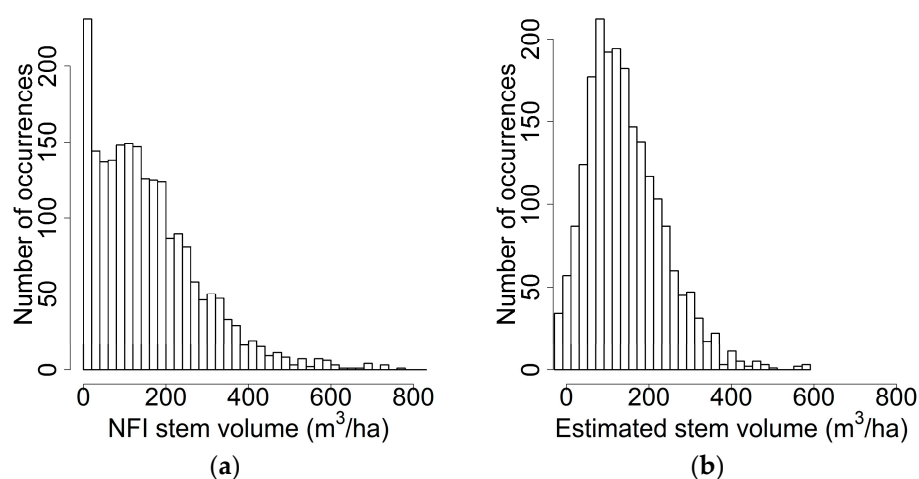


**Figure 16.** (a) The distribution of the field inventoried VOL. (b) The distribution of the modelled VOL using TanDEM-X data.

Both backscatter and scene temperature were also tested as explanatory variables, and they became significant at the 5% level from a strictly statistical perspective. However, they reduced the standard error only to a limited extent (1%–2% compared to excluding the variables), so in order to prioritize simplicity, only the phase height was used as the explanatory variables. The scatter plots of

the fitted models vs. reference data are illustrated in Figure 17. The SE was 29.4 tons/ha (34.3%) for the AGB model and 55.7 m<sup>3</sup>/ha (34.3%) for the VOL model, at the plot level.

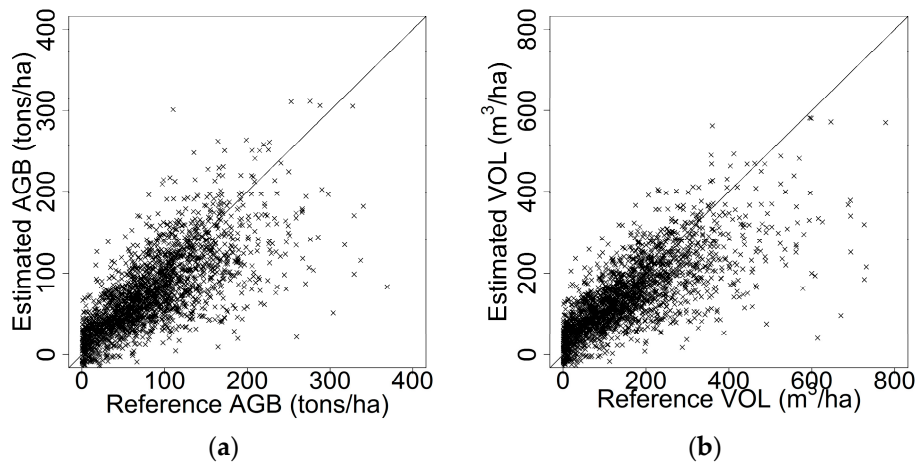


Figure 17. Estimated AGB (a) and VOL (b) from the NFI reference plots.

### 2.6.3. Assessment

The fitted models from the previous section were used to generate new AGB/VOL rasters covering the whole of Sweden. These were evaluated at the stand level using the three different datasets explained in Section 2.1.1. The RMSE was computed as [54]:

$$\text{RMSE} = \sqrt{\frac{\sum_{i=1}^n (\hat{X}_i - X_i)^2}{n}} \quad (9)$$

$$\text{RMSE}(\%) = \frac{\text{RMSE}}{\bar{X}} 100 \quad (10)$$

where  $n$  was the number of stands,  $\hat{X}_i$  was the value predicted from TanDEM-X data for stand  $i$  and  $X_i$  is the target value for stand  $i$ .  $\bar{X}$  represents the sampled mean for the variable in question. The bias was computed as:

$$\text{Bias} = \frac{\sum_{i=1}^n (\hat{X}_i - X_i)}{n} \quad (11)$$

where the variables and indices have the same meaning as before.

## 3. Results

Some stands available from the field reference data could not be evaluated, as they were located within the stripes of missing acquisitions (those with low HOA). Hence, the number of stands presented in Table 3 is lower than the amount of available stands presented in Table 1. The prediction accuracy was about 21%–23% for AGB and 24%–25% for VOL at all test sites (Table 3). There was no clear site dependence, and the relative accuracy of AGB and VOL was consistent for the two test sites where these data were available. This further confirms the strong correlation between the two variables AGB and VOL. The bias was below 10% at all test sites. At the test site in northern Sweden, the bias was 4.1% (AGB) and 4.3% (VOL), and for the large amount of forest stands spread across central Sweden, the bias was 2.3% (4.9 m<sup>3</sup>/ha). At the southern test site, the stands inventoried during 2017 stand out with a larger variance compared to the remaining ones. Despite the low overall bias, the AGB/VOL appear overestimated at lower volumes, while slightly underestimated at higher volumes (Figure 18). This might be a consequence of the selected model(s) without intercept, as illustrated in Figure 17. From that figure, one can suspect that the approximate intercept would be slightly above 0. Similarly,



the TanDEM-X observables appeared less sensible to higher volumes, which could be confirmed in Figures 18a–c and 19, where the predictions were slightly underestimated at higher volumes, but also had a larger spread.

**Table 3.** Evaluation statistics. Prediction accuracy (RMSE) and bias.  $n$  denotes the number of stands.

Test Site	Forest Attribute	RMSE	Bias	Unit	RMSE%	$n$
Northern Sweden	AGB	27.4	−6.17	tons/ha	23.4	11
Northern Sweden	VOL	55.3	−11.1	m <sup>3</sup> /ha	25.2	11
Central Sweden	VOL	52.4	4.90	m <sup>3</sup> /ha	25.0	222
Southern Sweden	AGB	29.7	10.5	tons/ha	20.8	15
Southern Sweden	VOL	65.1	23.1	m <sup>3</sup> /ha	24.1	15

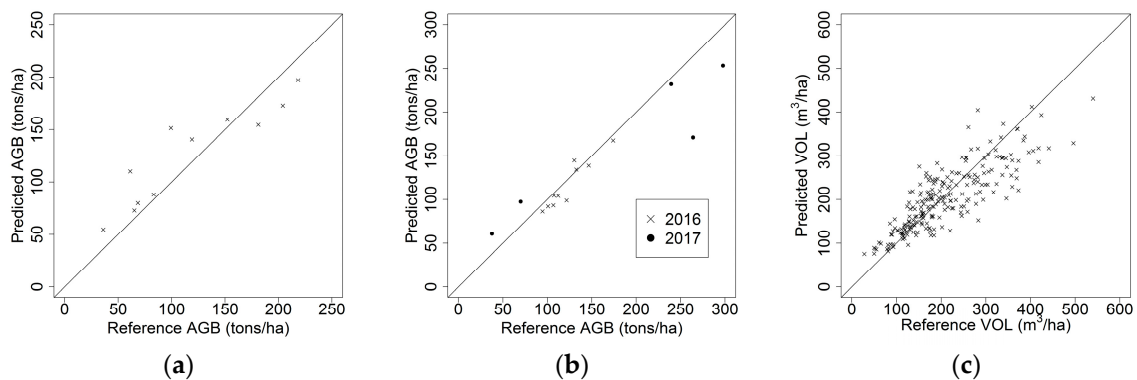


**Figure 18.** Evaluation of predicted AGB from TanDEM-X after growing season 2015 vs. (a) 11 field inventoried stands in northern Sweden 2016. (b) Fifteen field inventoried stands across southern Sweden. Ten stands were sampled with 10 plots/stand in 2016, while the remaining stands were sampled with 4 plots/stand in 2017. (c) Two hundred twenty two company inventoried stands in central Sweden.

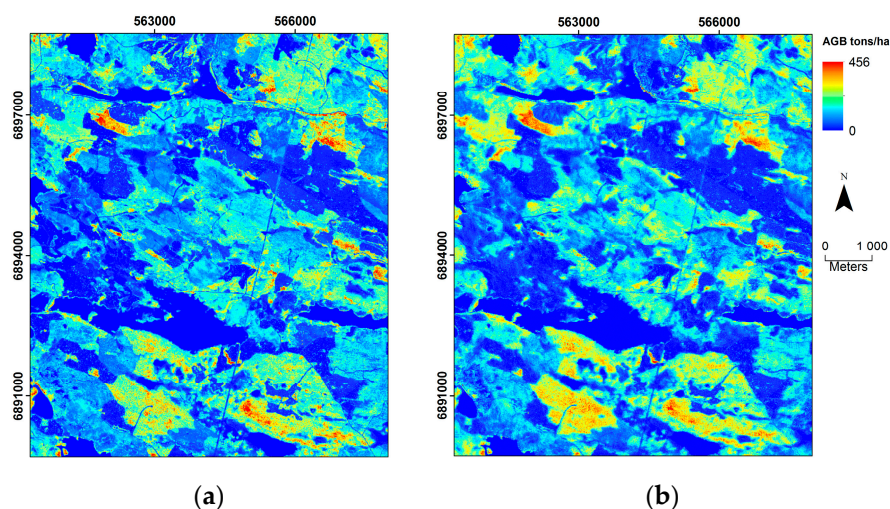


**Figure 19.** (a) ALS 2015-based AGB map by SLU and the Swedish Forest Agency [3] (b) TanDEM-X October 2015-based AGB map.

#### 4. Discussion

The first objective of this article includes spreading knowledge of the challenges and possible solutions and also suggesting further research questions about large-scale processing of TanDEM-X

InSAR data. The overall scheme for large-scale processing can follow an automated iterative approach of single scene processing, however, often with modifications depending on systematic circumstances of the region to be processed. For Swedish conditions, the long coast and widely different temperatures illustrate such challenges that have to be considered in addition to the processing of a single scene. Probably, it is even an advantage taking the processing apart, instead of first merging all SLC data into huge data stacks, as the large amounts of data will likely become a practical challenge for the hardware and software used.

The access to an accurate high resolution ALS DTM is however key to generate a continuous TanDEM-X product, without major gaps or jumps, by projecting the processed data onto the same continuous DTM. Nevertheless, the geocoding algorithm in the current approach did not always give good results. The geocoding was improved from the inherent SLC metadata by comparing TanDEM-X intensity images with the DTM. The intensity images did however contain the forest and everything above the DTM, as well, and this might partly explain the sometimes erroneous geolocation of the end product. At some regions, the correspondence was high ( $< 1$  pixel), and at some others, it was lower, being several pixels off, especially at forest borders and in hilly terrain. When compared to, for example, ALS data, these geolocation inaccuracies can be of crucial importance for the end user; but the problem is known, and solutions have been discussed for example in [55].

The normalization procedure of the backscatter, which included the pixel-area method, was important to be able to use the same backscatter levels from different scenes. The pixel-area method decreased the influence of hilly terrain, but it did still not improve the geolocation accuracy compared to working only with unprocessed intensity images. In this study, the backscatter from X-band did not contribute to the AGB/VOL estimations, most likely because of the short wavelength [12,56,57].

The phase height was the most important observable for the AGB/VOL estimation, and similar to earlier studies, it has shown strong correlation to AGB and also forest height [16,19,58–61]. The linear relation between phase height and stem volume appears similar to what was found in [21] (13.5 tons/ha/phase height meter change vs. 13.0; Figure 14 and Equations (7) and (8)). A major challenge with mosaicking phase heights appeared due to the phase trends appearing in most scenes, the origin of which could not be determined. The use of fitted polynomials to correct for this is a possible empirical correction approach giving satisfactory results, but with the need for improvements. As a similar trend appeared along the same orbits, an alternative processing approach might improve the phase height, by using the same parameters for all scenes with the same orbit. A robust algorithm to handle falsely unwrapped heights in scenes with an HOA causing ambiguities would decrease the requirements of certain acquisition settings.

Despite the coherence being significant as the explanatory variable, it was not used in the empirical model since the accuracy did not improve when it was included. However, the coherence had several crucial meanings during the processing. First and foremost, it is related to the quality of the phase height, and hence, it was also used in the derivation of the water mask. To avoid potentially masking out forest regions with low coherence (typically not a problem, but higher/denser forest generally decreases the coherence), both the coherence and the phase height might be used in conjunction, or one could simply use an external water mask. The interferometric coherence also has a strong relevance for AGB estimations, when other non-empirical approaches are used, such as the random volume over ground (RVoG), two-level model (TLM) or the interferometric water cloud model (IWCM), all of which have been proven to have good results [23–25,62,63]. The single coverage of Sweden required a compensation of the antenna gain loss against the scene sides, to stabilize the otherwise strong dependence on across-track location. The applied method (described in Section 2.3.3) was efficient, but should be further evaluated with regard to robustness and other possible weaknesses.

Both the phase height and coherence were clearly influenced by the temperature (or rather frozen/unfrozen conditions), where the phase height tended to decrease and the range of coherence decreased while the coherence showed a slight increase, but this relation should be clarified in future studies. This influence can for example be seen in Figure 11. However, by including the temperature

component in the processing, a tighter integration and correction with respect to the local conditions can be applied.

The second objective was to evaluate the accuracy at the stand level, and a large amount of stands from the entirety of Sweden was used for this. First, hundreds of company stands from central and southern Sweden were evaluated with respect to VOL. The RMSE (25.0%, Table 3) was low compared to some studies and higher compared to others, which have reported RMSEs in the range of about 15%–40% [16,18–23,59]. The robustness of the predictions was proven by the widely different locations across Sweden and also from scenes with higher and lower temperatures. The relevance also for AGB, and not only VOL, was proven by the evaluation in northern and southern Sweden, respectively, where both reference AGB and VOL were available. The similar results, 21%–25% RMSE, further confirmed the approximate quality that can be expected from TanDEM-X InSAR predictions, regardless of AGB/VOL. Pleasantly, the overall bias was low (Table 3), which is an important criterion to enable aggregation without increasing the bias as the region increases. Still, if anything, the lower VOLs tended to generally be overestimated while higher VOLs indicated a slight underestimation. This might also be due to that the datasets having been acquired mainly during winter conditions and definitely during leaf-off conditions. Hence, to gain an even more complete and fair evaluation, summer acquisitions should be evaluated, or perhaps only acquisitions with frozen ground conditions. The accuracy of these AGB/VOL maps (21%–25% RMSE) is higher than all earlier Swedish satellite-based nation-wide products, which generally have reported VOL accuracies of about 30%–80% RMSE at the stand level, and the accuracy is slightly lower than ALS-based maps (17%–22% RMSE) [3,9–11]. It seems natural to think that the greatly better accuracy in TanDEM-X- and ALS-based maps is due to the ability of acquiring 3D data, as the other maps were based on 2D data. The main advantage of using a satellite-based technique compared to airborne ones is that a new nation-wide coverage could be completed every four months, compared to every five years (assuming the same airborne technique), and hence, the current results are important to show how satellite-based maps can provide sufficient quality also for forest management purposes.

Generally, local errors detected in the mosaic could not be given priority of being corrected if no systematic error was found, and hence, large covering products like this mosaic will be slightly less accurate compared to a single scene processed only for a certain region, as more local adjustments can be considered. The mosaicking was quite rudimentary, and hence, the scene borders sometimes became prominent. An improved mosaicking, perhaps with block adjustments giving softer transitions, could improve the prediction quality and the appearance of a correct map without artefacts.

## 5. Conclusions

In this study, a set of 518 TanDEM-X scenes was interferometrically processed and mosaicked to the national level. In addition to traditional SAR processing steps, a number of challenging behaviours and adjustments were presented and discussed. Scenes acquired in frozen conditions (generally ground temperatures below 0 °C) showed a different behaviour, with lower phase heights and a smaller dynamic range of coherences. When possible, only scenes acquired with the same conditions should be used in order to facilitate the derivation of a correct phase height to volume function. Scenes covering the archipelago with isolated islands gained unwrapping clarity by defining a fixed near-zero phase in the surrounding water to achieve a continuous phase between the islands, which aided in avoiding phase jumps. This was not used for unwrapping of scenes in the inland, since the unwrapping efficiency was much improved by filtering the water bodies. The ground phase could not successfully be modelled from an ALS DTM, which introduced a phase trend across the scenes that had to be compensated against by fitting a 2D polynomial in open areas, where the phase heights and DTM should coincide. The reason for this scene trend could not be clarified, but it appeared to be different for different orbits and changed slowly along the orbits. The mosaicking was a simple layer-by-layer mosaic, which would likely take advantage of a proper block adjustment, to achieve smoother transitions between scenes. The geolocation accuracy was generally about 1–2 pixels, but in

some conditions larger. An improved geocoding would greatly enhance comparisons with other map products.

The SAR observables backscatter, phase height and coherence were extracted for 2288 NFI plot locations, spread across Sweden. The observables were used as explanatory variables in robust regression models, to explain the AGB and VOL, estimated from the inventoried NFI plots (10 m radius). The models were applied to the observable mosaics, to derive national AGB and VOL predictions. These maps were evaluated at the stand level on three independently inventoried datasets, spread across Sweden. It was found, that the relative RMSE was about 21%–25%, for all three datasets, corresponding to about 27–30 tons/ha or 52–65 m<sup>3</sup>/ha (Table 3). It was also found that the bias was low, despite a considerable standard deviation around the regression models. The accuracy was found sufficient for stand level purposes and is better than existing satellite-borne alternatives for frequent forest mapping at this scale. To conclude, TanDEM-X data are well suited for large-scale forest mapping, also for stand level purposes.

**Acknowledgments:** This study was financed by the European Community’s Seventh Framework Programme (FP7/2007–2013) under Grant Agreement No. 606971, the Advanced SAR project, the Swedish National Space Board through the project “Retrieval of forest biomass and biomass change with spaceborne SAR”, Contract No. 147/14, and by the Hildur & Sven Wingquist’s Foundation for Forest Research. The TanDEM-X images were acquired through the German Aerospace Center (DLR) “Large-scale biomass mapping of Sweden” project (XTI\_VEGE7029). The authors would like to acknowledge Emeritus Jan Askne and Mats Nilsson for valuable discussions. Matts Lindblad and Adam Felton are acknowledged for providing data from the south of Sweden.

**Author Contributions:** Henrik J. Persson carried out the SAR and some field data processing, the statistical analysis, put together the material and also wrote the majority of the paper. Håkan Olsson was involved in the statistical design. Maciej J. Soja contributed to the SAR processing and investigation of special cases. Lars M.H. Ulander was also involved in the research design and SAR processing. Johan E.S. Fransson was involved in the field data design and statistical design. All authors contributed to the writing.

**Conflicts of Interest:** The authors declare no conflict of interest.

## References

1. Næsset, E.; Gobakken, T.; Holmgren, J.; Hyypä, H.; Hyypä, J.; Maltamo, M.; Nilsson, M.; Olsson, H.; Persson, Å.; Söderman, U. Laser scanning of forest resources: The nordic experience. *Scand. J. For. Res.* **2004**, *19*, 482–499. [[CrossRef](#)]
2. Hyypä, J.; Hyypä, H.; Inkinen, M.; Engdahl, M.; Linko, S.; Zhu, Y.-H. Accuracy comparison of various remote sensing data sources in the retrieval of forest stand attributes. *For. Ecol. Manag.* **2000**, *128*, 109–120. [[CrossRef](#)]
3. Nilsson, M.; Nordkvist, K.; Jonzén, J.; Lindgren, N.; Axensten, P.; Wallerman, J.; Egberth, M.; Larsson, S.; Nilsson, L.; Eriksson, J.; et al. A nationwide forest attribute map of Sweden derived using airborne laser scanning data and field data from the national forest inventory. *Remote Sens. Environ.* **2017**, *194*, 447–454. [[CrossRef](#)]
4. Häme, T.; Salli, A.; Lahti, K. *Estimation of Carbon Storage in Boreal Forests Using Remote Sensing Data*; Academy of Finland: Helsinki, Finland, 1992.
5. Lei, Y.; Siqueira, P. An automatic mosaicking algorithm for the generation of a large-scale forest height map using spaceborne repeat-pass InSAR correlation magnitude. *Remote Sens.* **2015**, *7*, 5639–5659. [[CrossRef](#)]
6. Gruber, A.; Wessel, B.; Martone, M.; Roth, A. The TanDEM-X DEM Mosaicking: Fusion of Multiple Acquisitions Using InSAR Quality Parameters. *IEEE J. Sel. Top. Appl. Earth Obs. Remote Sens.* **2016**, *9*, 1047–1057. [[CrossRef](#)]
7. Reese, H.; Nilsson, M.; Sandström, P.; Olsson, H. Applications using estimates of forest parameters derived from satellite and forest inventory data. *Comput. Electron. Agric.* **2002**, *37*, 37–55. [[CrossRef](#)]
8. Tomppo, E.; Olsson, H.; Ståhl, G.; Nilsson, M.; Hagner, O.; Katila, M. Combining national forest inventory field plots and remote sensing data for forest databases. *Remote Sens. Environ.* **2008**, *112*, 1982–1999. [[CrossRef](#)]



9. Santoro, M.; Beaudoin, A.; Beer, C.; Cartus, O.; Fransson, J.E.S.; Hall, R.J.; Pathe, C.; Schmullius, C.; Schepaschenko, D.; Shvidenko, A.; et al. Forest growing stock volume of the northern hemisphere: Spatially explicit estimates for 2010 derived from Envisat ASAR. *Remote Sens. Environ.* **2015**, *168*, 316–334. [[CrossRef](#)]
10. Santoro, M.; Cartus, O.; Fransson, J.E.S.; Shvidenko, A.; McCallum, I.; Hall, R.J.; Beaudoin, A.; Beer, C.; Schmullius, C. Estimates of forest growing stock volume for sweden, central siberia, and québec using envisat advanced synthetic aperture radar backscatter data. *Remote Sens.* **2013**, *5*, 4503–4532. [[CrossRef](#)]
11. Santoro, M.; Beer, C.; Cartus, O.; Schmullius, C.C.; Shvidenko, A.; McCallum, I.; Wegmüller, U.; Wiesmann, A. The BIOMASAR algorithm: An approach for retrieval of forest growing stock volume using stacks of multi-temporal SAR data. In Proceedings of the ESA Living Planet Symposium, Bergen, Norway, 28 June–2 July 2010.
12. Dobson, M.; Ulaby, F. Dependence of radar backscatter on coniferous forest biomass. *IEEE Trans. Geosci. Remote Sens.* **1992**, *30*, 412–415. [[CrossRef](#)]
13. Rignot, E.; Way, J.; Williams, C.; Viereck, L. Radar estimates of aboveground biomass in boreal forests of interior Alaska. *IEEE Trans. Geosci. Remote Sens.* **1994**, *32*, 1117–1124. [[CrossRef](#)]
14. Rizzoli, P.; Bräutigam, B.; Kraus, T.; Martone, M.; Krieger, G. Relative height error analysis of TanDEM-X elevation data. *ISPRS J. Photogramm. Remote Sens.* **2012**, *73*, 30–38. [[CrossRef](#)]
15. Rossi, C.; Rodriguez Gonzalez, F.; Fritz, T.; Yague-Martinez, N.; Eineder, M. TanDEM-X calibrated Raw DEM generation. *ISPRS J. Photogramm. Remote Sens.* **2012**, *73*, 12–20. [[CrossRef](#)]
16. Persson, H.J.; Fransson, J.E.S. Comparison between TanDEM-X and ALS based estimation of above ground biomass and tree height in boreal forests. *Scand. J. For. Res.* **2017**, *32*, 306–319. [[CrossRef](#)]
17. Soja, M.J.; Persson, H.J.; Ulander, L.M.H. Estimation of forest height and canopy density from a single InSAR correlation coefficient. *IEEE Geosci. Remote Sens. Lett.* **2015**, *12*, 646–650. [[CrossRef](#)]
18. Treuhaft, R.; Gonçalves, F.; dos Santos, J.R.; Keller, M.; Palace, M.; Madsen, S.N.; Sullivan, F.; Graça, P.M. Tropical-Forest Biomass Estimation at X-Band From the Spaceborne TanDEM-X Interferometer. *IEEE Geosci. Remote Sens. Lett.* **2015**, *12*, 239–243. [[CrossRef](#)]
19. Kugler, F.; Schulze, D.; Hajnsek, I.; Pretzsch, H.; Papathanassiou, K.P. TanDEM-X Pol-InSAR Performance for Forest Height Estimation. *IEEE Trans. Geosci. Remote Sens.* **2014**, *52*, 6404–6422. [[CrossRef](#)]
20. Abdullahi, S.; Kugler, F.; Pretzsch, H. Prediction of stem volume in complex temperate forest stands using TanDEM-X SAR data. *Remote Sens. Environ.* **2016**, *174*, 197–211. [[CrossRef](#)]
21. Solberg, S.; Astrup, R.; Breidenbach, J.; Nilsen, B.; Weydahl, D. Monitoring spruce volume and biomass with InSAR data from TanDEM-X. *Remote Sens. Environ.* **2013**, *139*, 60–67. [[CrossRef](#)]
22. Karila, K.; Vastaranta, M.; Karjalainen, M.; Kaasalainen, S. Tandem-X interferometry in the prediction of forest inventory attributes in managed boreal forests. *Remote Sens. Environ.* **2015**, *159*, 259–268. [[CrossRef](#)]
23. Olesk, A.; Praks, J.; Antropov, O.; Zalite, K.; Arumäe, T.; Voormansik, K. Interferometric SAR Coherence Models for Characterization of Hemiboreal Forests Using TanDEM-X Data. *Remote Sens.* **2016**, *8*, 700. [[CrossRef](#)]
24. Askne, J.I.H.; Soja, M.J.; Ulander, L.M.H. Biomass estimation in a boreal forest from TanDEM-X data, lidar DTM, and the interferometric water cloud model. *Remote Sens. Environ.* **2017**, *196*, 265–278. [[CrossRef](#)]
25. Soja, M.J.; Askne, J.I.H.; Fellow, L.; Ulander, L.M.H. Estimation of Boreal Forest Properties from TanDEM-X Data using Inversion of the Interferometric Water Cloud Model. *IEEE Geosci. Remote Sens. Lett.* **2017**, *14*, 997–1001. [[CrossRef](#)]
26. Fridman, J.; Holm, S.; Nilsson, M.; Nilsson, P. Adapting National Forest Inventories to changing requirements—The case of the Swedish National Forest Inventory at the turn of the 20th century. *Silva Fenn.* **2014**, *48*, 1–29. [[CrossRef](#)]
27. Swedish National Forest Inventory. *Skogsdata 2013; Aktuella uppgifter om de svenska skogarna från Riksskogstaxeringen; Institutionen för skoglig resurshushållning, Sveriges Lantbruksuniversitet: Umeå, Sweden, 2013.*
28. Ranneby, B.; Cruse, T.; Hägglund, B.; Jonasson, H.; Swärd, J. *Designing a New National Forest Survey for Sweden*; Swedish University of Agricultural Sciences: Uppsala, Sweden, 1987.
29. Brandel, G. *Volymfunktioner för Enskilda Träd: Tall, Gran Och Björk = Volume Functions for Individual Trees: Scots Pine (Pinus Sylvestris), Norway Spruce (Picea Abies) and Birch (Betula Pendula & Betula Pubescens)*; Sveriges lantbruksuniversitet, Institutionen för skogsproduktion: Garpenberg, Sweden, 1990.



30. Marklund, L.G. *Biomassfunktioner för Tall, Gran Och Björk i Sverige*; Swedish National Forest Inventory: Umeå, Sweden, 1988.
31. Lindgren, O. Validation of stand-wise forest data based on ALS. In Proceedings of the Silvilar 2012, Vancouver, BC, Canada, 16–19 September 2012; pp. 1–8.
32. Rönnberg, A. *Kartografisk Information ur Laserdata*; Lantmäteriet: Gävle, Sweden, 2011; Volume 1.
33. Bergström, H.; Melin, H.; Nicolausson, A. *Höjddata—En Förutsättning för Klimatanpassning*; Swedish National Land Survey: Gävle, Sweden, 2009.
34. Solberg, S.; Weydahl, D.J.; Astrup, R. Temporal stability of X-band single-pass InSAR heights in a spruce forest: Effects of acquisition properties and season. *IEEE Trans. Geosci. Remote Sens.* **2015**, *53*, 1607–1614. [[CrossRef](#)]
35. Duque, S.; Balss, U.; Rossi, C.; Fritz, T.; Balzer, W. *TanDEM-X Payload Ground Segment: CoSSC Generation and Interferometric Considerations*; German Aerospace Center: Oberpfaffenhofen, Germany, 2012.
36. Wegmüller, U. Automated terrain corrected SAR geocoding. *IEEE Int. Geosci. Remote Sens. Symp.* **1999**, *3*, 1712–1714.
37. Small, D. Flattening gamma: Radiometric terrain correction for SAR imagery. *IEEE Trans. Geosci. Remote Sens.* **2011**, *49*, 3081–3093. [[CrossRef](#)]
38. Frey, O.; Santoro, M.; Werner, C.L.; Wegmüller, U. DEM-Based SAR Pixel-Area Estimation for Enhanced Geocoding Refinement and Radiometric Normalization. *IEEE Geosci. Remote Sens. Lett.* **2013**, *10*, 48–52. [[CrossRef](#)]
39. Bamler, R.; Hartl, P. Synthetic aperture radar interferometry. *Inverse Probl.* **1998**, *14*, 55. [[CrossRef](#)]
40. Hanssen, R.F. *Radar Interferometry: Data Interpretation and Error Analysis*, 2nd ed.; Springer: Dordrecht, The Netherlands, 2001.
41. Hagberg, J.O.; Ulander, L.M.H.; Askne, J. Repeat-pass SAR interferometry over forested terrain. *IEEE Trans. Geosci. Remote Sens.* **1995**, *33*, 331–340. [[CrossRef](#)]
42. Moreira, A.; Prats-Iraola, P.; Younis, M.; Krieger, G.; Hajnsek, I.; Papathanassiou, K. A Tutorial on Synthetic Aperture Radar. *IEEE Geosci. Remote Sens. Mag.* **2013**, *1*, 6–43. [[CrossRef](#)]
43. Goldstein, R.M.; Werner, C.L. Radar interferogram filtering for geophysical applications. *Geophys. Res. Lett.* **1998**, *25*, 4035–4038. [[CrossRef](#)]
44. Wegmüller, U.; Werner, C.L.; Strozzi, T.; Wiesmann, A. *Phase Unwrapping with GAMMA ISP Technical Report, 13-May-2002*; Gamma Remote Sensing: Bern, Switzerland, 2002.
45. Bachmann, M.; Schwerdt, M.; Alfonzo, G.C.; Schrank, D. Phase pattern calibration for interferometric applications in spaceborne SAR systems. *Int. J. Antennas Propag.* **2013**, *2013*. [[CrossRef](#)]
46. Chen, H.; Cloude, S.R.; Goodenough, D.G. Forest Canopy Height Estimation Using Tandem-X Coherence Data. *IEEE J. Sel. Top. Appl. Earth Obs. Remote Sens.* **2016**, *9*, 3177–3188. [[CrossRef](#)]
47. Zebker, H.A.; Villasenor, J. Decorrelation in interferometric radar echoes. *IEEE Trans. Geosci. Remote Sens.* **1992**, *30*, 950–959. [[CrossRef](#)]
48. Just, D.; Bamler, R. Phase statistics of interferograms with applications to synthetic aperture radar. *Appl. Opt.* **1994**, *33*, 4361–4368. [[CrossRef](#)] [[PubMed](#)]
49. Gonzalez, J.H.; Bachmann, M.; Krieger, G.; Fiedler, H. Development of the TanDEM-X calibration concept: Analysis of systematic errors. *IEEE Trans. Geosci. Remote Sens.* **2010**, *48*, 716–726. [[CrossRef](#)]
50. Solberg, S.; Lohne, T.-P.; Karyanto, O. Temporal stability of InSAR height in a tropical rainforest. *Remote Sens. Lett.* **2015**, *6*, 209–217. [[CrossRef](#)]
51. Cartus, O.; Santoro, M.; Schmullius, C.; Li, Z. Large area forest stem volume mapping in the boreal zone using synergy of ERS-1/2 tandem coherence and MODIS vegetation continuous fields. *Remote Sens. Environ.* **2011**, *115*, 931–943. [[CrossRef](#)]
52. Ruggero, B.; Ventura, L. An Introduction to Robust Estimation with R Functions. 2005. Available online: [https://www.google.ch/url?sa=t&rct=j&q=&esrc=s&source=web&cd=1&ved=0ahUKEwiQkN71yerXAhVJPFAKHSp-AncQFggsMAA&url=https%3A%2F%2Fwww.researchgate.net%2Ffile.PostFileLoader.html%3Fid%3D569bc60d6307d906458b45c8%26assetKey%3DAS%253A318926276235267%25401453049357465&usq=AOvVaw0N54DKxgwPk\\_zmo58QC3Uq](https://www.google.ch/url?sa=t&rct=j&q=&esrc=s&source=web&cd=1&ved=0ahUKEwiQkN71yerXAhVJPFAKHSp-AncQFggsMAA&url=https%3A%2F%2Fwww.researchgate.net%2Ffile.PostFileLoader.html%3Fid%3D569bc60d6307d906458b45c8%26assetKey%3DAS%253A318926276235267%25401453049357465&usq=AOvVaw0N54DKxgwPk_zmo58QC3Uq) (accessed on 12 October 2017).
53. Susanti, Y.; Pratiwi, H.; Sulistijowati, H.S.; Liana, T. M estimation, S estimation, and Mm Estimation in Robust Regression. *Int. J. Pure Appl. Math.* **2014**, *91*, 349–360. [[CrossRef](#)]

54. Hyndman, R.J.; Koehler, A.B. Another look at measures of forecast accuracy. *Int. J. Forecast.* **2006**, *22*, 679–688. [[CrossRef](#)]
55. Soja, M.J.; Ulander, L.M.H. Digital Canopy Model Estimation from TanDEM-X Interferometry Using High-resolution Lidar DEM. In Proceedings of the IEEE International Geoscience and Remote Sensing Symposium, Melbourne, Australia, 21–26 July 2013; pp. 165–168.
56. Imhoff, M.L. Radar backscatter and biomass saturation: Ramifications for global biomass inventory. *IEEE Trans. Geosci. Remote Sens.* **1995**, *33*, 511–518. [[CrossRef](#)]
57. Le Toan, T.; Beaudoin, A.; Riou, J.; Guyon, D. Relating forest biomass to SAR data. *IEEE Trans. Geosci. Remote Sens.* **1992**, *30*, 403–411. [[CrossRef](#)]
58. Solberg, S.; Astrup, R.; Gobakken, T.; Næsset, E.; Weydahl, D.J. Estimating spruce and pine biomass with interferometric X-band SAR. *Remote Sens. Environ.* **2010**, *114*, 2353–2360. [[CrossRef](#)]
59. Soja, M.J.; Persson, H.J.; Ulander, L.M.H. Estimation of boreal forest biomass from two-level model inversion of interferometric TanDEM-X data. In Proceedings of the IEEE International Geoscience and Remote Sensing Symposium, Quebec City, QC, Canada, 13–18 July 2014; pp. 3398–3401.
60. Praks, J.; Antropov, O.; Hallikainen, M.T. LIDAR-Aided SAR interferometry studies in boreal forest: Scattering phase center and extinction coefficient at X- and L-band. *IEEE Trans. Geosci. Remote Sens.* **2012**, *50*, 3831–3843. [[CrossRef](#)]
61. Soja, M.J.; Persson, H.J.; Ulander, L.M.H. Estimation of forest biomass from two-level model inversion of single-pass InSAR data. *IEEE Trans. Geosci. Remote Sens.* **2015**, *53*, 5083–5099. [[CrossRef](#)]
62. Askne, J.I.H.; Fransson, J.E.S.; Santoro, M.; Soja, M.J.; Ulander, L.M.H. Model-based biomass estimation of a hemi-boreal forest from multitemporal TanDEM-X acquisitions. *Remote Sens.* **2013**, *5*, 5574–5597. [[CrossRef](#)]
63. Caicoya, A.T.; Kugler, F.; Hajnsek, I.; Papathanassiou, K.P. Large-Scale Biomass Classification in Boreal Forests With TanDEM-X Data. *IEEE Trans. Geosci. Remote Sens.* **2016**, *54*, 5935–5951. [[CrossRef](#)]



© 2017 by the authors. Licensee MDPI, Basel, Switzerland. This article is an open access article distributed under the terms and conditions of the Creative Commons Attribution (CC BY) license (<http://creativecommons.org/licenses/by/4.0/>).